HYBRID AND ELECTROMAGNETIC LARGE BANDWIDTH ENERGY HARVESTERS WITH INTERFACE CIRCUIT FOR 0.4-1.6 G ACCELERATION RANGE

A THESIS SUBMITTED TO
THE GRADUATE SCHOOL OF NATURAL AND APPLIED SCIENCES
OF
MIDDLE EAST TECHNICAL UNIVERSITY

BY

AKIN MERT YILMAZ

IN PARTIAL FULFILLMENT OF THE REQUIREMENTS
FOR
THE DEGREE OF MASTER OF SCIENCE
IN
ELECTRICAL AND ELECTRONIC ENGINEERING

APRIL 2023

Approval of the thesis:

HYBRID AND ELECTROMAGNETIC LARGE BANDWIDTH ENERGY HARVESTERS WITH INTERFACE CIRCUIT FOR 0.4-1.6 G ACCELERATION RANGE

submitted by **AKIN MERT YILMAZ** in partial fulfillment of the requirements for the degree of **Master of Science** i**n Electrical and Electronic Engineering, Middle East Technical University** by,

Prof. Dr. Halil Kalıpçılar
Dean, Graduate School of **Natural and Applied Sciences** _____

Prof. Dr. İlkay Ulusoy
Head of the Department, **Electrical and Electronics Eng.** _____

Prof. Dr. Haluk Külah
Supervisor, **Electrical and Electronics Eng., METU** _____

Examining Committee Members:

Prof. Dr. Tayfun Akın
Electrical and Electronics Eng., METU _____

Prof. Dr. Haluk Külah
Electrical and Electronics Eng., METU _____

Assoc. Prof. Dr. Yeşim Serinağaoğlu Doğrusöz
Electrical and Electronics Eng., METU _____

Assoc. Prof. Dr. Ender Yıldırım
Mechanical Engineering, METU _____

Assoc. Prof. Dr. Dinçer Gökcen
Electrical and Electronics Eng., Hacettepe University _____

Date: 25.04.2023

I hereby declare that all information in this document has been obtained and presented in accordance with academic rules and ethical conduct. I also declare that, as required by these rules and conduct, I have fully cited and referenced all material and results that are not original to this work.

Name Last name : Akın Mert Yılmaz

Signature :

ABSTRACT

HYBRID AND ELECTROMAGNETIC LARGE BANDWIDTH ENERGY HARVESTERS WITH INTERFACE CIRCUIT FOR 0.4-1.6 G ACCELERATION RANGE

Yılmaz, Akın Mert
Master of Science, Electrical and Electronic Engineering
Supervisor : Prof. Dr. Haluk Külah

April 2023, 77 pages

Environmental energy sources such as vibration, heat and light can be converted to electrical energy by energy harvesters and stored in batteries and super-capacitors using interface circuits (IC). Depending on the size and application of the energy harvester, a 50 cm^3 transducer can supply power at the level of mWs, which is enough for new-generation integrated sensors and systems developed with deep sub-micron technology. Hence, with the help of energy harvesters, it is possible to operate sensors and systems in closed environments without charging and maintenance. However, an essential part of the vibration sources does not generate vibrations at a constant frequency and acceleration level, which creates a need for energy harvesters with bandwidth ratios above 20% which can generate power from vibrations with a wide range of acceleration levels (0.4-1.6 g). Furthermore, different vibration sources may require application-specific energy harvester designs whose electrical characteristics vary. To convert generated AC electrical energy from distinct energy harvesters to storable energy, an IC, which can adapt itself to the electrical characteristics of the energy harvester to harvest energy at the optimum level, is necessary. The goal of this thesis study is to design and implement systems that can harvest energy from human body motions and mechanical vibrations.

The designed hybrid energy harvester can harvest human body vibrations within the 1-2 Hz frequency range at 0.4-1.6 g using the proposed frequency up-conversion method. The proposed electromagnetic energy harvester (EMEH) has a large frequency bandwidth of 22.9-29.7 Hz at 1.4 g acceleration with a bandwidth ratio of 28%. Experimental results show that the designed EMEH can output 12.3 mW power with a normalised power density (N.P.D) of 0.22 ($mW/cm^3/g^2$) at 1 g input acceleration.

Finally, an interface IC is designed and implemented in TSMC 180 nm technology. Simulation results of the sub-blocks of the interface show that with the proposed method, energy can be harvested from a large frequency spectrum and regulated for the sensors of interest.

Keywords: Electromagnetic energy harvester, hybrid energy harvester, vibration-based energy harvesting, maximum power point tracking, interface circuit.

ÖZ

0.4-1.6 G İVME ARALIĞI İÇİN GENİŞ BANT GENİŞLİKLİ HİBRİT VE ELEKTROMANYETİK ENERJİ TOPLAYICILARI VE ARAYÜZ DEVRESİ

Yılmaz, Akın Mert
Yüksek Lisans, Elektrik ve Elektronik Mühendisliği
Tez Yöneticisi: Prof. Dr. Haluk Külah

Nisan 2023, 77 sayfa

Titreşim, ısı ve ışık gibi çevresel enerji kaynakları, enerji toplayıcılar tarafından elektrik enerjisine dönüştürülebilir ve arabirim devreleri (IC) kullanılarak bataryalarda ve süper kapasitörlerde depolanabilir. Enerji hasat cihazının boyutuna ve uygulamasına bağlı olarak, 50 cm^3 hacminde bir transdüser, derin submikron teknolojisi ile geliştirilmiş yeni nesil entegre sensörler ve sistemler için yeterli olan mW seviyesinde gücü sağlayabilir. Böylece, enerji toplayıcılar sayesinde sensörlerin ve sistemlerin kapalı ortamlarda şarj ve bakım gerektirmeden çalıştırılması mümkündür. Ancak titreşim kaynaklarının önemli bir kısmı sabit bir frekans ve ivme seviyesinde titreşim üretmez, bu da çok çeşitli ivme seviyelerine (0,4-1.6 g) sahip titreşimlerden güç üretebilen, bant genişliği oranları %20'nin üzerinde olan enerji toplayıcılara ihtiyaç yaratır. Ayrıca, farklı titreşim kaynakları, elektriksel karakteristikleri değişen ve uygulamaya özel enerji toplayıcı tasarımına gerek duyabilmektedir. Farklı enerji toplayıcılardan üretilen alternatif akım elektrik enerjisini depolanabilir enerjiye dönüştürmek için, enerji toplayıcının elektriksel özelliklerine uyum sağlayabilen ve optimum düzeyde enerji toplayan bir entegre devre gereklidir. Bu tez çalışmasının amacı, insan vücudunun hareketlerinden ve mekanik titreşimlerden enerji elde edebilen sistemler tasarlamak ve üretmektir.

Tasarlanan hibrit enerji toplayıcı, önerilen frekans yükseltme yöntemini kullanarak 1-2 Hz frekans aralığında ve 0,4-1,6 g ivme seviyesindeki insan vücudu titreşimlerini toplayabilir. Önerilen elektromanyetik enerji toplayıcı (EMET), %28'lik bir bant genişliği oranıyla 1,4 g ivmedeki titreşimler için 22,9-29,7 Hz'lik geniş bir frekans bant genişliğine sahiptir. Deneysel sonuçlar, tasarlanan EMET'in 1 g titreşim ivmesinde, 0,22 ($mW/cm^3/g^2$) normalleştirilmiş güç yoğunluğu (N.G.Y.) ile 12,3 mW güç üretebileceğini göstermektedir.

Son olarak, TSMC 180 nm teknolojisinde bir arayüz entegre devresi tasarlanmış ve üretilmiştir. Arayüzün alt bloklarının simülasyon sonuçları, önerilen yöntemle enerjinin geniş bir frekans spektrumundan toplanabileceğini ve ilgili sensörler için düzenlenebileceğini göstermektedir.

Anahtar Kelimeler: Elektromanyetik enerji toplayıcı, hibrit enerji toplayıcı, titreşim temelli enerji toplama, maksimum güç noktası takibi, arayüz devresi.

To my universe,

seems dark but full of stars

ACKNOWLEDGMENTS

First and foremost, I want to thank Prof. Dr. Haluk Külah for his supervision, guidance, and support during my academic career. I am glad to be given the opportunity to be part of this research group, where I met people who touched and changed my life.

I would like to thank Prof. Dr. Tayfun Akın, Assoc. Prof. Dr. Yeşim Serinağaoğlu Doğrusöz, Assoc. Prof. Dr. Ender Yıldırım and Assoc. Prof. Dr. Dinçer Gökcen for being a part of my thesis jury and for their guidance.

I would like to thank Dr. Aykan Batu, Dr. Hasan Uluşan, Dr. Mahmut Kamil Aslan and Dr. Salar Chamanian for their guidance and help during my graduate work.

I would like to thank my colleagues and friends in the BioMEMS Research Group, Aziz Koyuncuoğlu, Ali Can Atik, Berat Yüksel, Berkay Çiftçi, Beyhan Türkyılmaz, Cansu Aslantürk, Dicle Balcı, Feyza Pirim, Mert Doğan, Mert Koç, Özlem Topçu and Zeynep Çağlayan for their friendships and collaborations.

I would like to offer my special thanks to Andaç Yiğit and Yasemin Engür for being my dear friends and always being there for me when I am in need.

I would like to thank all my friends Anıl, Berkay, Cigo, Ece, Emir, Gülin, Şeker and Zak, who motivated me to finish my thesis and always supported me mentally.

Finally, I would like to thank my family, especially to my little Pof, for being there for me.

This author is financially supported by TUBITAK BIDEB 2210-A 2020-1 Scholarship during this study.

This work has received funding from the European Research Council (ERC) under the European Union's Horizon 2020 research and innovation programme (Grant No:682756).

TABLE OF CONTENTS

LIST OF TABLES

TABLES

LIST OF FIGURES

FIGURES

CHAPTER 1

INTRODUCTION

"Internet of Things (IoT)" is a growing technology in our world. IoT is basically controlling any device with an on-and-off switch via the internet. This concept can be applied to a wide variety of devices which mainly consist of equipment used by humans on a daily basis, such as lamps, heating systems, dishwashers, TV, and coffee machine. Since IoT primarily focuses on human life and makes people's life easier, it found a place in the technology market and grew immensely. According to [1], there will be 75 billion installed IoT units by 2025, nearly a threefold increase from 2019 data.

IoT is limited by stand-alone devices, often connected to other sensors or gadgets. However, a new concept named "Internet of Everything (IoE)" proposes wireless sensors and actuators very small that they can disappear in any device, product or even the human body. The driving forces behind IoE are ultra-low power processors, low-cost ultra-low power sensors and low-power wireless connectivity technologies such as Bluetooth Low Energy (BLE). According to the power consumption data of MEMS (Micro-electromechanical systems) sensors and TI BLE module taken from [2-3], interested MEMS sensors can operate with μW level power consumption and BLE module consume μW level power when idle and mW level power when active, depending on the connection duration and frequency as shown in Table 1.1.

Table 1.1 Power Consumption Data of MEMS, Sensors and BLE module [2-3].

Product	**Supply Voltage**	**Supply Current**	**Device Size**
LIS2DW12 Accelerometer	1.7-3.6 V	50nA idle 1 µA active	2.8 mm^3
MP23AB01DH MEMS Microphone	2.3-3.6 V	220 µA	8.2 mm^3
STLM20 Analog Temperature Sensor	2.4-5.5 V	4.8 µA	UDFN-4L 1.3 mm^2
TI CC2541 BLE	3.3 V	1 µA idle 8.25mA (Single RX TX operation for 2.7 ms)	QFN40 36 mm^2

IoE comes with a power supply problem since being small becomes unimportant if the power is supplied to the sensors from a comparably bulky battery. Ultra-low power technologies behind the sensors and processors bring the opportunity for these devices to work with the harvested energy from the environment with mm^3 or cm^3-sized energy harvesters, which brings a solution to the bulky battery problem.

Removing batteries from the equation, the question of which harvestable energy source to use arises. Our living environment has many renewable and environmentally friendly energy sources such as heat, solar, kinetic and electromagnetic energy. There are mature techniques to harvest those renewable energy sources on a large scale with solar panels, wind tribunes, magnetic actuators etc. However, harvesting energy on a small scale to power up MEMS and sensors makes those mature energy harvesting techniques ineffective or inapplicable [4].

Aiming to find a solution to such problems, much research has been done on energy harvesting technology for self-sustainable sensors and MEMS. However, more than

this research is required since harvested energy should be converted to regulated DC power.

This thesis aims to design electromagnetic and hybrid(electromagnetic-piezoelectric) energy harvesters for energy scavenging from car engine vibrations and human body motions, respectively. Furthermore, blocks of the interface electronics for rectifying the input and performing MPPT (Maximum Power Point Tracking) will be designed using TSMC 180nm technology.

This chapter provides an introduction to harvestable energy sources, vibration energy harvesting methods and their interface electronics. Section 1.1 focuses on harvestable energy sources and gives detail on mechanical vibration sources that can be used. Sections 1.2 and 1.3 briefly explain the operation principles of electromagnetic and piezoelectric energy harvesters, respectively. Section 1.4 summarises the operation of the vibration-based energy harvester interface electronics on a system level. Lastly, Section 1.5 outlines the organisation of the thesis.

1.1 Harvestable Energy Sources

The different forms of energy that can be acquired from natural resources such as wind, water, vibration, geothermal heat, and biomass are referred to as harvestable energy sources. As we attempt to lessen our reliance on nonrenewable energy sources such as fossil fuels, these sources are becoming increasingly significant. Recent technological advances have allowed exploiting these resources on a broader scale than ever before. Wind turbines and solar panels, for example, are becoming more efficient and cost-effective, enabling increasing usage of these technologies to generate electricity. Advances in energy storage technologies have also enabled the storage of energy generated by wind and solar power for usage during peak demand periods. With continued research and development, there is potential for even further improvements in the efficiency and cost-effectiveness of harvestable energy sources,

making them an increasingly viable option for meeting our energy needs. Nevertheless, those harvested energies show different characteristics in different conditions, which makes it challenging to design a reliable and stable energy harvester for wearable and size&weight limited applications. Data on harvestable energy by energy harvesters in different conditions [4] can be seen in Table 1.2.

Table 1.2 Performance of energy harvesters under different environmental conditions [4].

Energy Harvester	**Power Densities**	
	Indoor Conditions	**Outdoor Conditions**
Solar panel	100μW/cm^2 @10W/cm^2	10mW/cm^2 @STC
Wind turbine-generator	35μW/cm^2 @<1m/s	3.5mW/cm^2 @8.4m/s
Thermoelectric generator	100μW/cm^2 @5 C gradient	3.5mW/cm^2 @30 C gradient
Electromagnetic generator	4μW/cm^3 @human motion-Hz 800μW/cm^3 @machine-kHz	

As shown in Table 1.2, the harvestable energy density for solar, wind, and thermal energy harvesting may vary significantly with environmental circumstances. Though it appears that electromagnetic energy harvesting from mechanical vibrations also varies significantly with vibration frequency, harvesters can be made to operate at their best within a specific frequency range. This circumstance also poses additional difficulties for the development of electromagnetic energy harvesters, such as selecting the best operating frequency and monitoring and assessing environmental vibrations.

1.1.1.1 Mechanical Vibrations

In our daily lives, vibration sources can come from a wide range of sources and are everywhere. These sources include environmental vibrations, such as those brought on by wind, earthquakes, and traffic, as well as mechanical vibrations brought on by tools, motors, and pumps. Walking, running, and jumping are examples of human activities that might cause vibrations. In addition, the frequency and amplitude of vibration sources might change based on the source and its surroundings. For the purpose of creating efficient vibrational energy harvesters that can catch and transform these vibrations into usable electrical energy, it is essential to comprehend the properties and behaviour of various vibration sources. For that purpose, vibration measurement data under different conditions are presented in Table 1.3.

Table 1.3 Acceleration magnitude and frequency of fundamental vibration mode for various sources [5]

Vibration source	**Acceleration (g)**	**F_{peak} (Hz)**
Car engine compartment	1.22	200
The base of the 3-axis machine tool	1.02	70
Blender casing	0.65	121
Clothes dryer	0.36	121
A person nervously tapping their heel	0.31	1
Car instrument panel	0.31	13
Door frame just after the door closes	0.31	125
Small microwave oven	0.25	121
HVAC vents in an office building	0.02-0.15	60
Windows next to a busy road	0.07	100
CD on notebook computer	0.06	75
Second story floor of a busy office	0.02	100

As shown in Table 1.3, rotating and moving machines such as a car engine, 3-axis machine tool, and blender can produce vibrations at higher frequencies and accelerations than other tiny devices or human motion. It is also evident that the distance from the vibration source influences the vibration's characteristics. Human motions should be considered as a vibration source for wearable device applications. Human motion generates vibrations with varying characteristics based on the source of the vibration (ankle, wrist, waist, etc.) and the type of motion (walking, running, swinging, etc.). According to [6-7], human mobility generates harvestable vibrations with a frequency spectrum of 1.2-3 Hz and an acceleration of 0.3-3.2 g. Table 1.4 displays the data on human body vibration characterisation acquired from [6-7].

Table 1.4 Acceleration spectrum for human body movements

Measurement Location	Movement Type	Frequency (Hz)	Acceleration (g)
Wrist	Walking	1.2-2	0.3-0.6
Wrist	Running	2.8-3	1.2-2.2
Waist	Walking	1.7-2	0.3-0.7
Waist	Running	2.5-3	1.1-2.6
Ankle	Walking (4m/s)	1.8-2	3.2 (peak)

Based on the facts in Table 1.4, it can be concluded that the greatest power can be generated by ankle movement since swing acceleration and range of the foot are greater than other portions of the body. However, the energy harvester should be developed with the end user in mind. Despite the fact that foot movement produces more power, hands are utilised more frequently in daily life, making them a more stable power source than the foot. Also, the end user's physical activity should be properly evaluated, and if necessary, other environmental vibration sources such as functioning mechanical devices, autos, and so on should be harvested. This raises the issue of broadband operation for electromagnetic energy harvesters, as they often have a resonance frequency at which they operate optimally.

1.2 Electromagnetic Energy Harvesters

The electrical energy generation principle of electromagnetic energy harvesters is based on Faraday's law of induction (1.1). The magnetic field encompassed by the coil changes with the relative movement of a conducting coil and a permanent magnet, and a voltage is induced at the conductor terminals. The induced voltage is proportional to the rate of change of the flux and velocity. The flux change is directly proportional to the number of coil turns and magnet parameters. Furthermore, the overall system architecture, magnet and coil arrangement, and area enclosed by each coil turn all have a substantial impact on system performance.

$$\varepsilon = -\frac{d\emptyset}{dt} = \oint_C \mathbf{E} \cdot d\mathbf{l} = -\frac{d}{dt}\int_S \mathbf{B} \cdot d\mathbf{S} \qquad (1.1)$$

Figure 1.1.a depicts a tubular electromagnetic harvester with a moving magnet that conducts the harvesting operation described. The magnet moves across the tube in one direction as a result of the vibration, changing the flux passing through the coil. This motion generates an emf whose amplitude is determined by the vibration's acceleration as well as coil turn number, area, magnet mass, spring constant, resonance frequency, and so on. Figure 1.1.b depicts the electromagnetic harvester model from Figure 1.1.a. The solution to this model is explained in detail in Section 2.1.

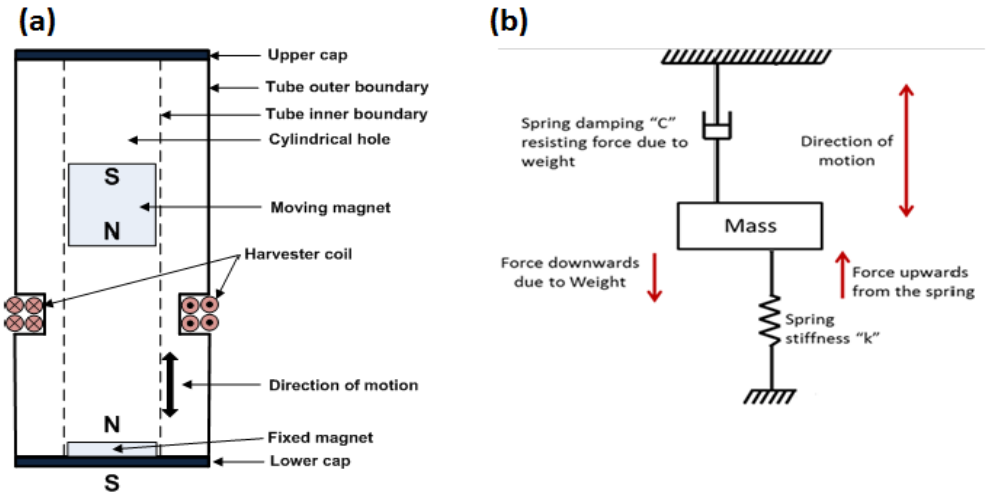

Figure 1.1. a) Tubular, moving magnet, electromagnetic energy harvester b) Spring, mass, damper model of the electromagnetic energy harvester [6].

1.3 Piezoelectric Energy Harvesters

Lead zirconate titanate (PZT) is a common piezoelectric material used in vibrational energy harvesters. Vibration causes deformation of the piezoelectric material in piezoelectric harvesters. This strain on PZT causes charge displacement between the top and bottom plates of the PZT layer (direct piezoelectric action), resulting in an AC voltage. Figure 1.2 depicts the piezoelectric effect with dipole polarisation in a PZT crystal [8], [9].

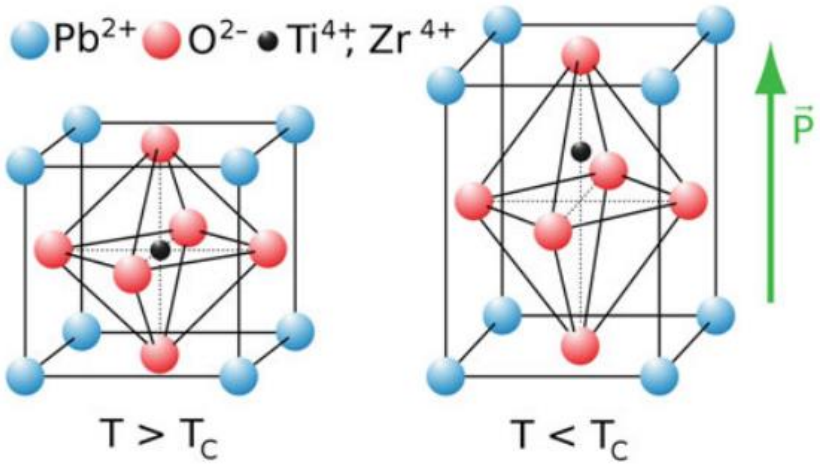

Figure 1.2. Intrinsic piezoelectric effect in lead zirconate, showing the crystallite above and below the Curie temperature T_C, where the charged zirconium or titanium ion moves relative to the center position [8].

Piezoelectric materials are often stiff (inflexible). When fastened directly to the frame and used as PEHs, this results in impractically high resonance frequencies. As a result, as shown in Figure 1.3 [8], PZT is coated on a cantilever beam to construct a simple energy-harvesting mechanical structure. In this picture, a mass is added at the tip of the cantilever beam to the lower resonance frequency, allowing IC designers to create efficient interface circuit topologies.

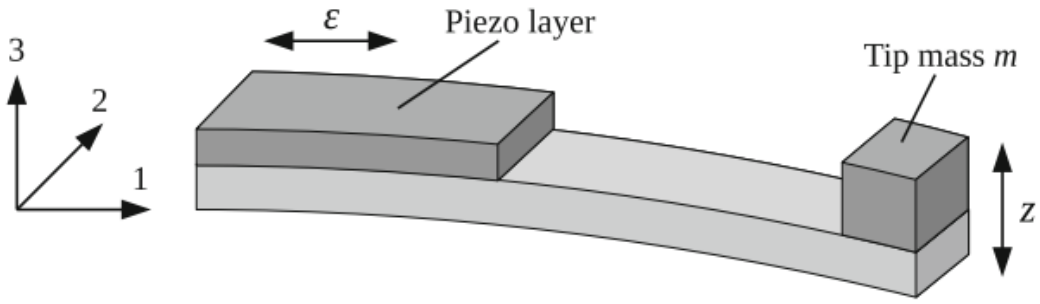

Figure 1.3. Cantilever structure converting the displacement z in the 3 direction into an elongation ε in the 1 direction.

Compressive and tensile strains caused by cantilever beam movement concentrate around the fixed end of the beam opposite the tip mass. As a result, a piezo layer is

glued to the fixed end to transform the majority of these pressures into electrical energy. Spring-mass-damper model of PEHs is similar to electromagnetic energy harvesters and it is explained in section 2.2

1.4 Interface Electronics for Vibration-based Energy Harvesters

A vibration-based energy harvester's performance is determined by various elements, including the transducer material, the mechanical resonator, and the interface electronics. The interface electronics are in charge of turning the transducer's electrical output into a useful source of power. The interface electronics, in particular, must match the transducer's impedance to the load and provide a sufficient level of power conditioning to guarantee that the output voltage and current are within the intended range. Furthermore, the interface electronics must be built to enhance power transfer efficiency and minimise power losses while simultaneously providing overload and short-circuit safety. In the literature, several interface electronics architectures have been proposed, ranging from simple diode-based rectifiers to more complicated active circuits that incorporate voltage multipliers, DC-DC converters, and maximum power point trackers. The design and optimisation of interface electronics is a vital stage in the construction of an efficient and effective vibrational electromagnetic energy harvesting system. In Chapter 3, a generic system block diagram of a vibration-based energy harvester interface is shown, and its sub-blocks are detailed in depth.

1.5 Objective of the Thesis

The goal of this thesis is to design and implement energy harvesters for wearable applications and car engine vibrations. Then designing the sub-blocks of interface electronics that converts the AC voltage output of the vibration to a regulated DC voltage. The objectives of this thesis are listed as follows:

1. Analyzing and determining the properties of harvestable vibrations from human body motions and car engines. Then using the obtained vibration data to design energy harvesters suitable for applications.
2. Mitigating the energy harvesting problems of the applications. In this regard, proposing a frequency up-conversion method to overcome the interface electronic's low-frequency vibration harvesting challenge. Also, implementing a method to increase the energy harvesting bandwidth so that varying the vibration frequency of the car engine does not prevent the energy harvesting operation.
3. Designing interface electronics sub-blocks that can be utilised to have a cold start, AC/DC conversion, MPPT (impedance matching) and multi-stage operation capability to operate with different input voltages (0.3-7 V).
4. Testing the designed transducers in a controlled laboratory environment.

1.6 Outline of the Thesis

The rest of the thesis consists of 4 chapters. Chapter 2 describes the operation principles of electromagnetic and piezoelectric energy harvesters. The literature review focuses on reaching the objectives mentioned in section 1.5. Finally, the design and operation principles of proposed hybrid and electromagnetic energy harvesters are explained in this chapter.

Chapter 3 starts with an introduction to the overall system of interface electronics and explains the operations of sub-blocks. Then focuses on the schematic and layout design of the sub-blocks of the proposed energy harvester interface electronics design and their simulations.

Chapter 4 starts with analysing car vibration frequency and amplitude spectrum and continues with controlled shaker table experiments of the designed and implemented energy harvesters with determined test conditions according to source vibration analysis.

Chapter 5 concludes the thesis by reviewing the results of this work and outlining probable future areas for research on this topic.

CHAPTER 2

VIBRATION-BASED ELECTROMAGNETIC AND HYBRID ENERGY HARVESTERS

Piezoelectric (PZT), electrostatic, and electromagnetic (EM) conversion methods are widely utilised to generate energy from vibration [10-14]. Among these methods, piezoelectric and electromagnetic energy harvesters yield the most efficient results in terms of power density. However, electromagnetic and piezoelectric energy harvesting have different shortcomings depending on their applications. Two critical design challenges of the electromagnetic energy harvesters operate at low-frequency vibrations, e.g., vibrations arising from the movements of the human body can be listed as (i) low voltage output due to the low acceleration amplitude of the vibration and (ii) the output power density is directly proportional to the device size which is not helpful in wearable applications where a portable and comfortable design is essential. The problem with piezoelectric energy harvesters is their cantilevered structure, whose length is inversely proportional to the resonance frequency. Hence, the cantilever length should be increased to reduce the piezoelectric energy harvester's resonance frequency, which is also not desirable for wearable applications. On the other hand, resonance frequency and displacement amplitude are inversely proportional in electromagnetic energy harvesters, given that acceleration amplitude is constant. The energy harvester design should be designed to tolerate low vibration displacement amplitudes to harvest energy from low acceleration vibrations.

This chapter describes the operation principles of electromagnetic, piezoelectric, and hybrid energy harvesters in Sections 2.1-2.3. Energy harvester requirements are determined for wearable applications, and a hybrid energy harvester design is

proposed for human body vibrations in section 2.4. Section 2.5 proposes a nonlinear electromagnetic energy harvester design with an improved energy harvesting frequency bandwidth. The 3D design&printing process of this nonlinear electromagnetic energy harvester is explained, and finally, an FEM analysis of the coil-magnet structure is performed.

2.1 Electromagnetic Energy Harvesters

Magnetic materials are subjected to Faraday's law of electromagnetic induction to generate electrical energy from electromagnetic and kinetic energy. The voltage generated by electromagnetic induction can be formulated as in equation 1.1. A voltage can be generated according to Faraday's law using a structure of a moving ferromagnet in the central axis of a coiled diamagnet (copper).

To have a better magnetic flux change rate, a resonant dynamic system should be constructed with magnetic and coil structures. Each dynamic system can be modelled as a mass-spring-damper model. A second-order mass-spring-damper model can be used for linear electromagnetic vibration energy harvesters (EVEH), whose representation is presented in Figure 2.1.

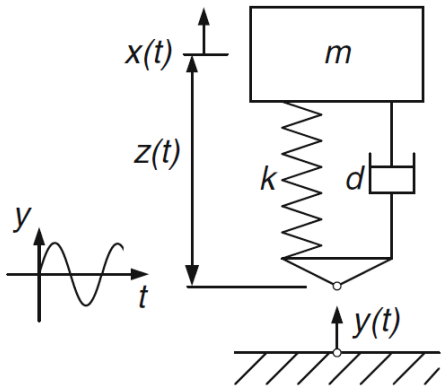

Figure 2.1. Linear electromagnetic energy harvester model [15].

A simplified analytical model of an electromagnetic harvester can be governed by a mass-spring-damper-based equation of motion relations. Lei et al. and Hasani et al.

[35], [26] governed the analytical model for the electromagnetic harvester with a detailed damping model. When his model is simplified and integrated into the linear electromagnetic energy harvester model, the following equations can be obtained:

$$m\ddot{z}_m + d\dot{z}_m + k_{mag}(z_m) = m\ddot{y}_b(t) \qquad (2.1)$$

In equation 2.1, m, d, and k are the notations for the total mass, total damping, and total stiffness of the system, respectively. For the described analytical model, it is assumed that the vibration direction is in the orthogonal direction to the magnets, denoted with y(t), and z is used for denoting the relative motion of the coils with respect to the outer frame.

Systems response is examined under the harmonic response of $y(t) = Y_0 \sin(\omega t)$ where ω is denoted as applied harmonic input frequency, and a steady solution is obtained as follows:

$$z(t) = \frac{(\frac{\omega}{\omega_n})^2 Y_0}{\sqrt{\left(1-(\frac{\omega}{\omega_n})^2\right)^2 + \left(2(\zeta_e + \zeta_m)\frac{\omega}{\omega_n}\right)^2}} \sin(\omega t - \varphi) \qquad (2.2)$$

In equation 2.2, $\omega_n = \sqrt{k/m}$ and $\zeta = \zeta_e + \zeta_m = d/2m\omega_n$ which are natural frequency and damping factor (electrical and mechanical), respectively. Rewriting equation 1, emf output of a linear electromagnetic energy harvester can be expressed in terms of the displacement z(t) as in equation 2.3, where k_t is the transduction factor.

$$\varepsilon = -\frac{d\emptyset}{dt} = -\frac{d\emptyset}{dz}\frac{dz}{dt} = k_t \frac{dz}{dt} \qquad (2.3)$$

Using equation 2.3, an electromagnetic energy harvester is designed and proposed in Section 2.5.

Several techniques that improve optimum power generation were reported in the literature recently. For example, Kwon et al. [19] increased power generation by replacing the moving magnet in the conventional linear electromagnetic energy harvester with magnets with the same poles facing each other. In such a structure,

magnets repel each other, creating a magnetic field on the horizontal axis that increases the radial magnetic field. Additionally, the direction of the flux between each subsequent layer will be opposite. Therefore, the flux in the coil changes multiple times, which is proportional to the number of stacked magnet layers, in a half cycle of the input vibration shown in Figure 2.2. Another advantage of the proposed system is that higher power can be outputted from low-frequency vibrations (<5 Hz) compared to single magnet electromagnetic energy harvesters because electromagnetic energy harvester is similar to an ac generator and with increased magnetic flux oscillation frequency; ac power is generated more efficiently. This system can generate an average of 980 µW power from vibration with an acceleration amplitude of 1 m/s2 and a frequency of 4.1 Hz.

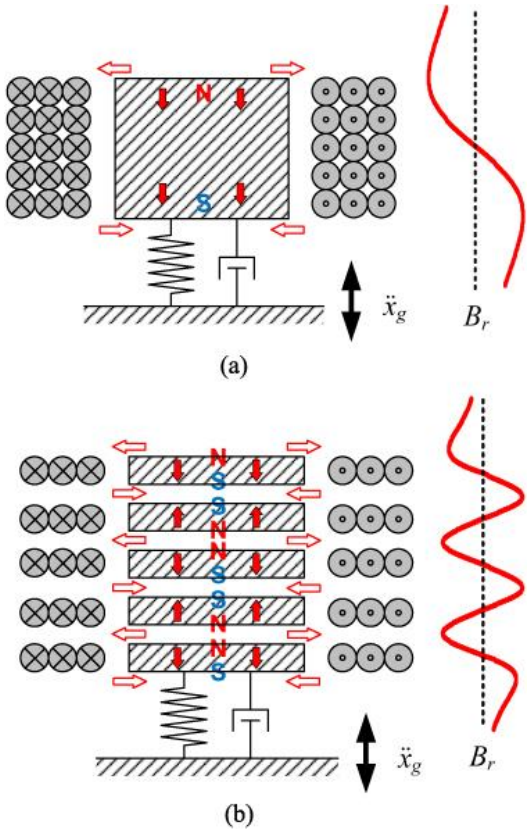

Figure 2.2. Magnet structures and radial magnetic flux density of electromagnetic energy harvesters. (a) Conventional single magnet and coil. (b) Repulsively stacked multilayer magnets and independent coils. [19].

Figure 2.3 represents an electromagnetic energy harvester that generates high power at low-frequency vibrations [21]. The harvester utilises the frequency up-conversion method by transferring the input vibration energy to the cantilever beam structure. Although the structure that the magnet is attached to vibrates at a low frequency, in each half cycle of its vibrations, it excites the cantilever beam structure of the coil. In this way, the vibration frequency is increased to the resonance frequency of the beam by using the momentum of the moving magnet. The presented system produced an average of 540 µW of power from vibration with an acceleration amplitude of 11.9 m/s2 and a frequency of 10 Hz.

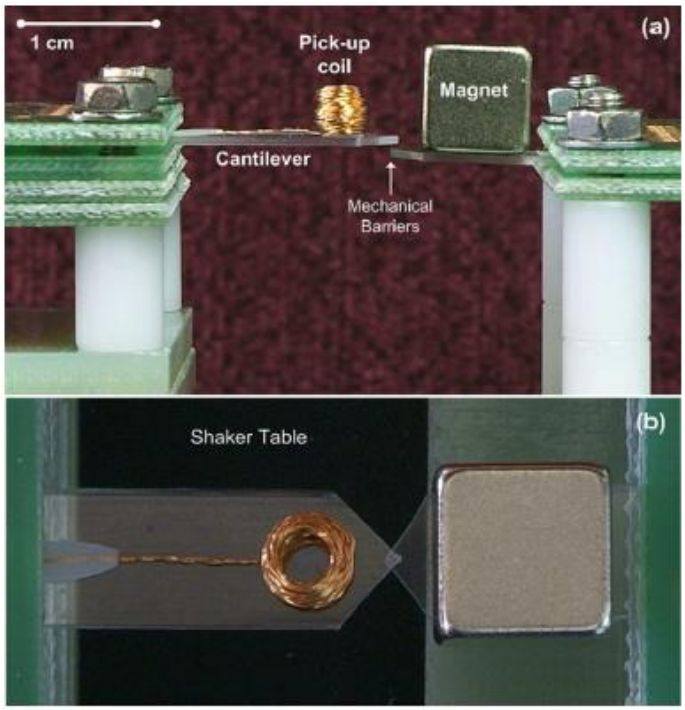

Figure 2.3. Electromagnetic energy harvester based on Frequency Up-conversion Method [21].

2.2 Piezoelectric Energy Harvesters

Similar to electromagnetic energy harvesters, piezoelectric energy harvesters can be modelled mechanically. For example, the piezoelectric energy harvester (PEH) in the form of a cantilever beam structure (Figure 2.4) can also be modelled as in Figure 2.1 [15].

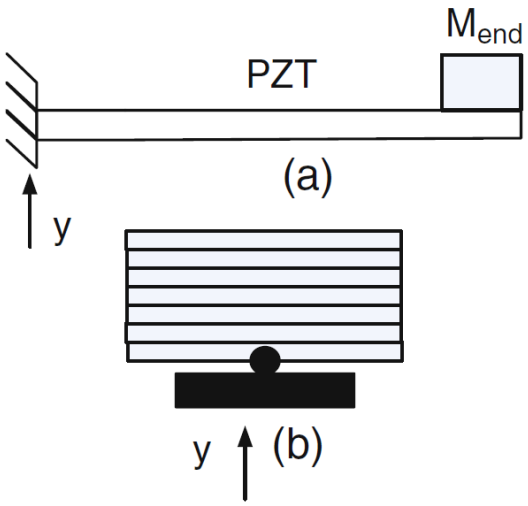

Figure 2.4. Piezoelectric cantilever beam energy harvester structure [16].

The resonance frequency of cantilever beams ω_n can be expressed as in equations 2.4 and 2.5, where K is the spring coefficient, M is the equivalent mass of the model in Figure 2.1, E is the elasticity coefficient, I is the moment of inertia, and L is the beam length.

$$the\ \omega_n = \sqrt{\frac{K}{M}} \qquad (2.4)$$

$$K = \frac{3EI}{L^3} \qquad (2.5)$$

The vibrations originating from human body movements such as running, jogging, or walking have frequencies around 2 Hz. To use piezoelectric energy harvesters in

this low-frequency range, mechanical stops that limit the motion of the vibrating mass can be used (Figure 2.5) [17].

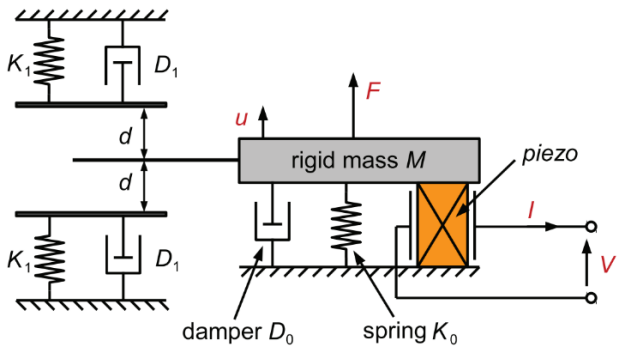

Figure 2.5. Piecewise linear structure of the piezoelectric energy harvester [17].

However, in such a system, the energy loss in the mechanical stops causes a loss in the total generated power. More specifically, frequency-dependent vibration amplitude curves of energy harvesting systems with and without mechanical stops are illustrated in Figure 2.6.

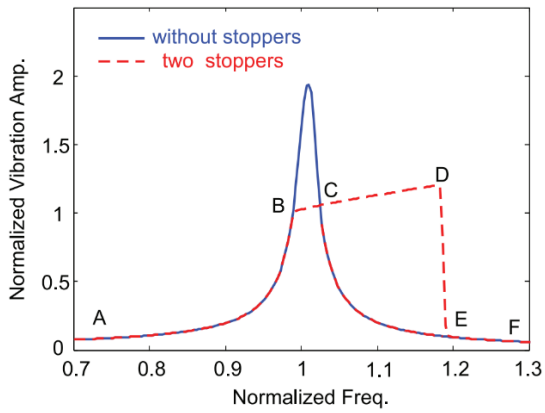

Figure 2.6. Frequency amplitude graph of piezoelectric energy harvesters with and without mechanical stop [17].

In this figure, the decrement in the vibration amplitude can be explained by using the piecewise linear energy harvester structure. The frequency responses of the systems with and without stoppers are the same from points A to B since the vibration amplitude at frequencies lower than point B is smaller than the constrained distance (d) in Figure 2.5. As the vibration amplitude reaches the determined limit of (d)

between B and D, it will start to deform, and the vibration amplitude will start to differ from the linear structure. At point E, since the frequency increases, the vibration amplitude will remain below the specified limit (d), and the system will return to its linear model.

According to the results obtained by Wu et al. [17], while the power produced decreases due to the limit in vibration amplitude (d), the harvestable vibration energy frequency bandwidth is increased to 20% of the energy harvester's resonance frequency (Figure 2.6).

2.3 Hybrid Energy Harvesters

As aforementioned, electromagnetic and piezoelectric energy harvesters have advantages over each other. Piezoelectric energy harvesters have a low coupling coefficient and low dependence on load resistance. In contrast, electromagnetic energy harvesters have a higher ohmic loss, which they compensate for with high coupling coefficients. In this regard, electromagnetic energy harvesters can operate as current pumps by yielding high currents. In contrast, the performance of piezoelectric energy harvesters is less affected by the load resistance than electromagnetic energy harvesters. Recently, hybrid energy harvesters have been designed to combine these two advantages.

Liu et al. [22] used the structure of a beam fixed at two ends with a magnet attached at its centre and two coils with spring magnets aligned above and below the centre magnet (Figure 2.7). In this system, a non-linear vibration movement is achieved with permanent magnets placed on the upper and lower parts of the energy harvester. Therefore, the energy harvesting frequency range has become adjustable with the distances of the permanent magnets. However, the disadvantage of this system is the high operating frequencies (39.3-130 Hz) compared to human movements. The system generated an average of 10.5 mW power from vibration with an acceleration amplitude of 5.9 m/s^2 and a frequency of 111 Hz.

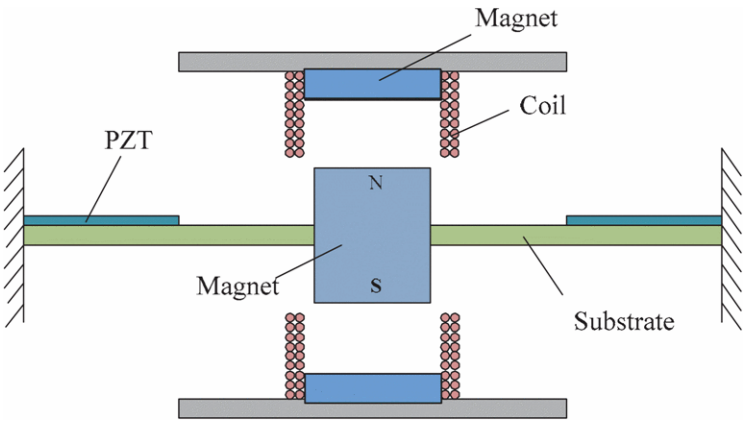

Figure 2.7. Hybrid piezoelectric and electromagnetic energy harvester [22].

As summarised in Table 2.1, large-volume electromagnetic energy harvesters [23] yield better results in terms of normalised power density compared to small-volume energy harvesters. Since large energy harvesters have magnets with larger surface area and mass, electromagnetic energy harvesters require high operation frequencies to generate power more efficiently. The systems introduced in [19] and [21] compensate for this disadvantage by utilising different frequency amplification methods.

Piezoelectric energy harvesters have lower volumes than electromagnetic energy harvesters. However, they still have higher power densities compared to electromagnetic energy harvesters owing to their high operating frequencies. To this end, combining electromagnetic energy harvesters with piezoelectric energy harvesters that utilise frequency amplification methods will increase the power density without increasing the volume significantly.

Table 2.1 Piezoelectric, electromagnetic and hybrid energy harvester experiment results.

Reference	Energy Harvesting Method	Energy Harvester Volume (cm^3)	Vibration Frequency (Hz)	Vibration Acceleration (g)	Max. Power (mW)	Power Density (mW/cm^3)	Normalised Power Density ($mW/cm^3/g^2$)
Amirtharajah [13]	EM	23.5	2	0.3	0.4	0.017	0.16
Wu [17]	PZT	-	87	1.2	2.1	-	-
Berdy [18]	PZT	0.58	50	0.2	0.105	0.18	4.5
Kwon [19]	EM	18.1	4.1	0.1	0.98	0.054	5.25
Zorlu [21]	EM	2.96	10	1.21	0.76	0.255	0.17
Liu [22]	Hybrid	-	111	0.6	10.5	-	-
Yamaguchi [23]	EM	123	2	0.2	18.7	0.15	5.9
Galchev [24]	EM	43	2	1	0.057	0.0013	0.057

2.4 Hybrid Energy Harvester for Wearable Applications

2.4.1 Energy Harvester Requirements

Hybrid energy harvester (HEH) design specifications have been determined by considering the end user's requirements. Hence, human motions should be considered a vibration source for wearable device applications. Since human body vibrations are not fixed at a single frequency and may vary over time, the energy harvester should have a large frequency bandwidth. Human motions create vibrations with different characteristics depending on the vibration source (ankle, wrist, or waist) and motion type (walking, jogging, or running). The vibration created by the running movement aimed at collecting energy was investigated in [31].

Figure 2.8 shows the wireless sensor node employed to characterise wrist vibration. In this structure, the movement of the wrist is independent of the body movement and investigated in two axes, perpendicular to the arm (vertical) and parallel to the arm (forward).

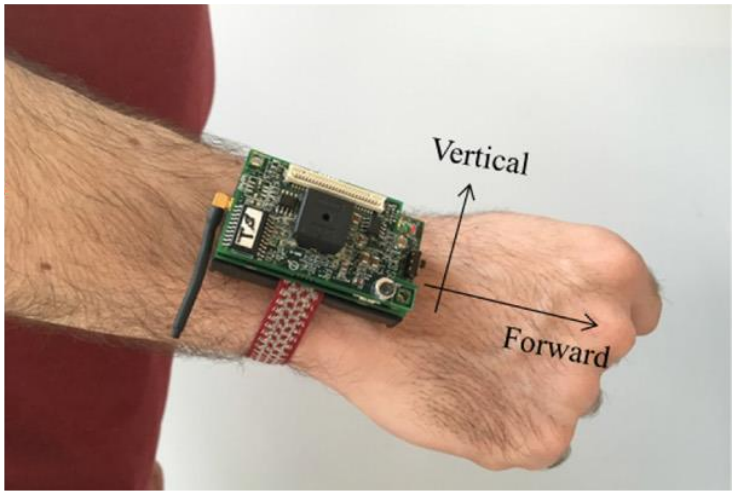

Figure 2.8. Wrist vibration characterization mechanism [31].

Wrist vibration features characterised using the wireless sensor node, and accelerometer are illustrated in Figure 2.9. The feature characterisation results highlight that vibrations occur in the wrist in the range of 2.8-3 Hz. Additionally, vertical acceleration is more prominent than forward acceleration.

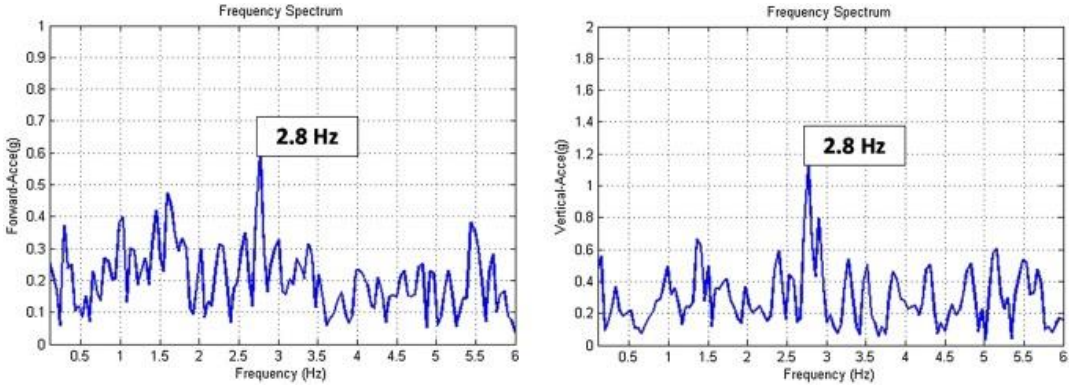

Figure 2.9. Frequency spectra of vertical and forward wrist vibration accelerations [31].

The frequency spectra show that the vibrations are dominant around 2.8 Hz, and the frequencies of these vibrations change depending on the running speeds and different users. To this end, increasing the bandwidth has become necessary to obtain high power from the vibrations of each user.

Another feature that should be included in the design is making the piezoelectric springboard energy harvester, which has a higher resonance frequency than the wrist vibration frequency and is operable at 2.8 Hz. To explain the reason for this requirement, one should refer to the resonant frequency equations of the cantilever beam structure expressed in equations 2.4 and 2.5.

As seen in (2.4), in order to decrease the resonance frequency of the cantilever beam structure to the human body frequency range, the equivalent mass (M) must be increased. Therefore, the tip mass of the cantilever beam must be increased. However, if the tip mass is much higher than the mass of the cantilever beam, the structure may deteriorate during vibration. Another resonant frequency reduction method is to decrease the spring coefficient (K). As can be observed from the equation in (2.5), this can be achieved by increasing the length of the cantilever beam structure, assuming that the elasticity coefficient (E) is maintained. However, increasing the length of the cantilever beam negatively affects the wearability character of the energy harvester.

2.4.2 Proposed Energy Harvester and Working Principle

A novel hybrid energy harvester is designed considering the requirements mentioned earlier.

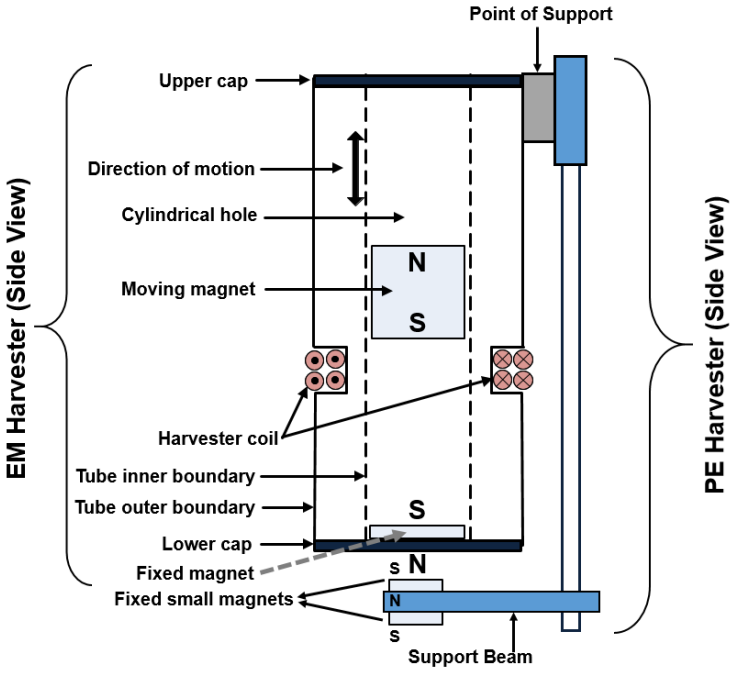

Figure 2.10. Proposed original hybrid energy harvester design.

A vital aspect of this design is an electromagnetic energy harvester (EMEH), which generates energy from low-frequency vibrations using Faraday's law, and a piezoelectric energy harvester, which has a higher resonance frequency the EMEH, operates at the same input vibrations. The principle of conservation of momentum was used to combine electromagnetic and piezoelectric energy harvesters. However, the force relation between magnets should be investigated before explaining the hybrid harvesting operation principle.

Vokoun et al. [32] expressed the force between two identical magnets of equal length as:

$$F_z = -\frac{\pi.\mu_0.M.R^4}{4}\left[\frac{1}{x} + \frac{1}{(x+2t)^2} - \frac{2}{(x+t)^2}\right] \qquad (2.6)$$

Where R is the magnet radius, t is the length of the magnet, and x is the distance between the magnets. As seen from Figure 2.10, the repulsion force between the moving and the fixed lower cap magnet will increase when the moving magnet moves towards the bottom cover. This movement also increases the repulsion force

between the fixed small magnets at the tip of the piezoelectric cantilever beam structure and the moving magnet. If all of the magnets in the structure were identical, the repulsive force between the moving magnet and the fixed piezoelectric tip magnets could not be larger than the pulling force between the permanent magnets. Therefore, the cantilever beam structure would not be able to move. However, the moving magnet is much larger than the tip magnets, which enables the cantilever beam structure to move. The force diagram between the magnets is shown in Figure 2.11.

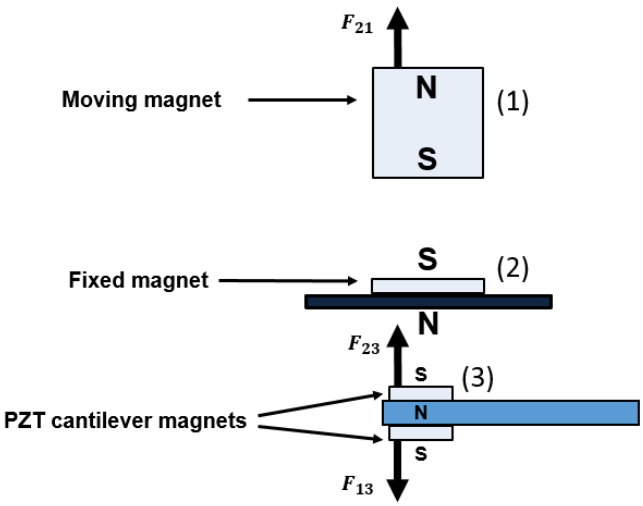

Figure 2.11. Force diagram between hybrid energy harvesting magnets.

If the forces between the magnets (F_{21}, F_{13}, F_{23}) in Figure 2.11 are investigated, $F_{21}>F_{23}>F_{13}$ when the first magnet approaches the second magnet. At a certain distance, forces on the third magnet become $F_{13}>F_{23}$, and the piezoelectric cantilever beam magnets are pushed away from the energy harvester body (Figure 2.12).

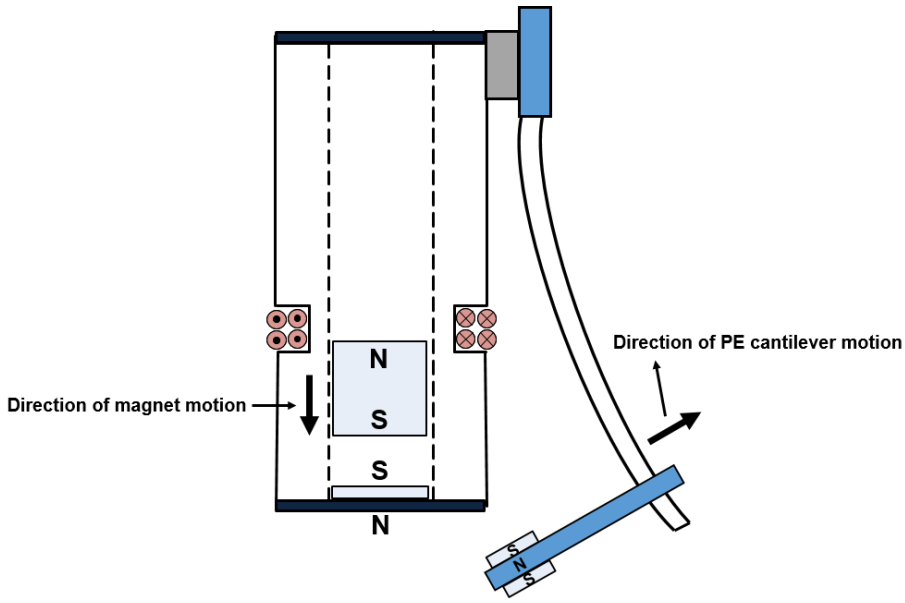

Figure 2.12. The bending diagram of the cantilever beam as a result of the moving magnet approaching the cover magnet.

The impact between the moving magnet and cantilever beam magnets can be modelled as a non-ideal elastic collision. In this collision, the moving magnet transferred some of its moment to the piezoelectric cantilever beam magnets. The piezoelectric cantilever beam magnets' momentum moves the beam's tip, creating tension at the cantilever beam's base. The piezoelectric material converts this tension to voltage and, therefore, into electrical energy. During this movement, the moving magnet passes through the coil and generates a voltage according to Faraday's law of electromagnetic induction in (1.1). The spring energy stored in the cantilever beam forces the beam towards the electromagnetic energy harvester structure. When the velocity of the piezoelectric cantilever beam is zero, there is a net force on the beam towards the EMEH structure. The cantilever beam, accelerated by this force, collides with the EMEH structure, as in Figure 2.13, as the moving magnet moves away from the lower cap.

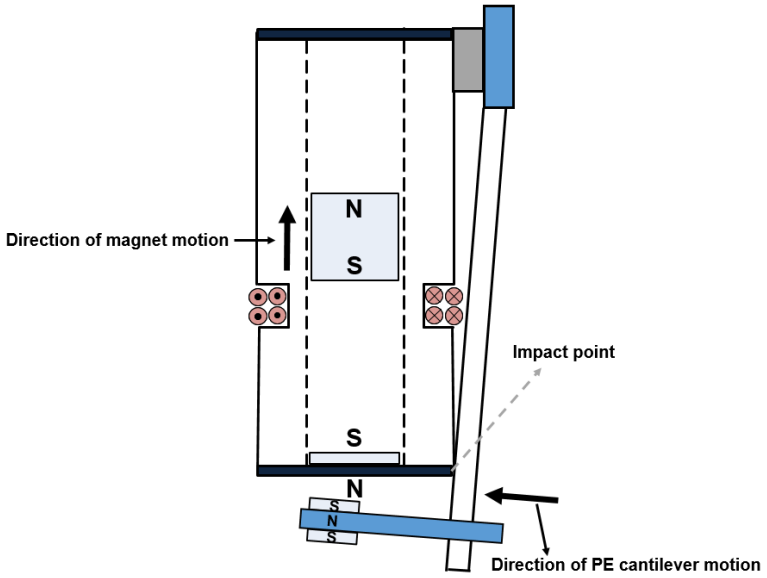

Figure 2.13. State diagram of the magnets in the hybrid energy harvester and the cantilever beam as a result of the release of the mechanical energy stored in the cantilever beam.

As a result of the collision, the piezoelectric cantilever beam structure generates sinusoidal vibrations damped over time at its resonance frequency. Owing to this frequency up-conversion method, the problem of matching the wrist vibration frequency with the natural frequency of the piezoelectric cantilever beam structure is mitigated. The hybrid energy harvester produced according to the created design is shown in Figure 2.14.

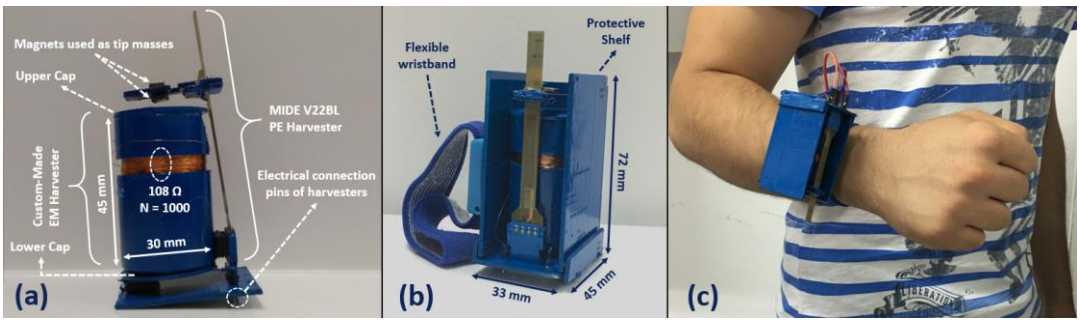

Figure 2.14. Hybrid energy harvester a) open construction b) in a protective sheath c) on the wrist

2.4.3 Piezoelectric Energy Harvester Characterization

As mentioned in section 2.4.2, the frequency up-conversion method utilised in the developed HEH is based on the impact of the cantilever beam structure on the EMEH structure. During this impact, the cantilever beam structure bounces off the EMEH body until its mechanical energy is dissipated. In such an impact, two different situations occur. Firstly, the cantilever beam structure moves away from the body and shows the characteristic of the cantilever beam fixed at one end, whose stiffness equation can be derived as in (2.7) [33]. In the second situation, the cantilever beam structure is in contact with the EMEH body and vibrates as a beam fixed at both ends, which has a stiffness equation as expressed in (2.8) [33]. The 64-fold increment in the stiffness equation forms the basis of the second frequency up-conversion in the HEH.

$$k_z = \frac{1}{4}\frac{Ewh^3}{L^3} \tag{2.7}$$

$$k_z = 16\frac{Ewh^3}{L^3} \tag{2.8}$$

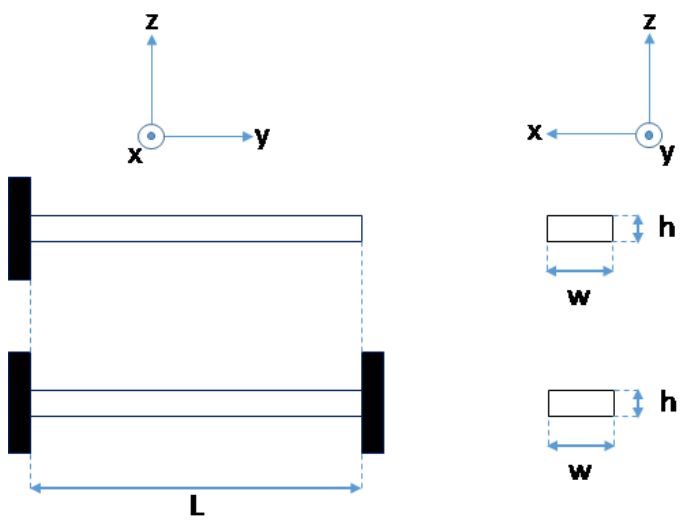

Figure 2.15. Two states of the Piezoelectric Energy Harvester after hitting the EMEH body. Cantilever beam structure fixed at one end (top), cantilever beam structure fixed at both ends (bottom).

The piezoelectric energy harvester (PEH) used in the HEH is the V22BL model produced by MIDE. Its dimensions can be seen in Figure 2.16a. Its natural frequency depends on the mass attached at its tip, as shown in Figure 2.16b, and it is in the range of 30 to 110Hz. This frequency is much higher than the frequency band of excitation from wrist movement (between 1.5-3 Hz). This means that a direct excitation by the wrist movement will not be sufficient to put the cantilever beam in resonance and thus will produce meagre power.

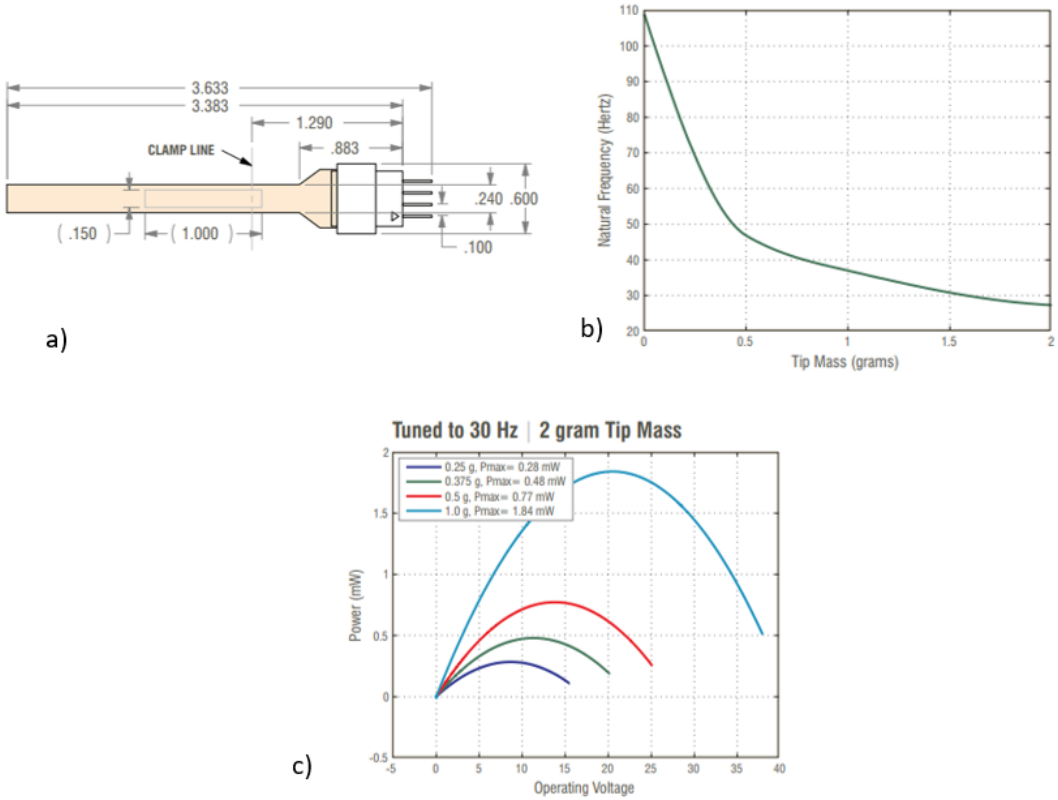

Figure 2.16. MIDE V22BL characteristics. a) PEH structure and dimensions (inches). b) Natural Frequency and End Mass graph. c) PEH Power and Operating Voltage graph with a tip mass of 2 grams tuned to a natural frequency of 30 Hz.[34]

Using the data in Figure 2.16b, the PEH is tuned to a natural frequency of 23Hz using a 2.25 grams tip mass. According to the producer's data in Figure 2.16c, the V22BL generates about 1.84 mW under an acceleration of 1g @30Hz. The PEH was characterised by the "Transducer Characterization Assembly" mentioned in section

4.1. The characterisation can be summarised as connecting various load resistances to the PEH output and performing a frequency sweep with the shaker table. The optimum resistive load for energy harvesting was found to be 238 kΩ, as shown in Figure 2.17. The PEH generated 1.94 mW power under an acceleration of 1g @23 Hz, which is consistent with the producer datasheet.

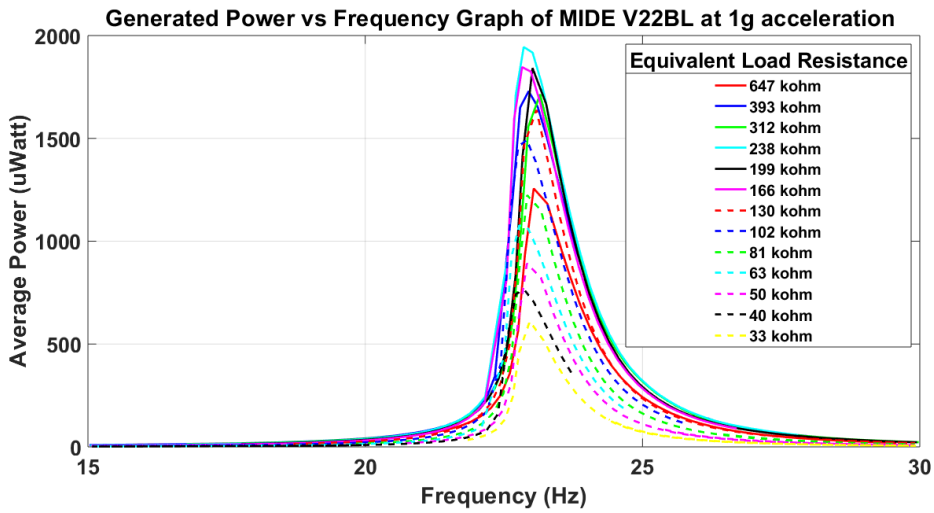

Figure 2.17. Generated Power and Frequency Graph of the MIDE V22BL vibrating with a 2.25 g tip mass and 1 g acceleration.

2.5 Large Bandwidth Electromagnetic Energy Harvester

According to the vibration measurement performed on a car, which is explained in section 4, the engine generates vibration in the range of 15-30 Hz and multiples of this range with 0.5-2 g acceleration amplitude. This broad frequency bandwidth of 15 Hz (proportional to the vibration frequency) creates a requirement for a large bandwidth energy harvester.

Another design parameter is the output power of the harvester. To have a basic idea of the output power of linear electromagnetic energy harvesters, equation 2.9, published by Williams and Yates in [38], should be analysed.

$$P = \frac{m\zeta_e(\frac{\omega}{\omega_n})^3\omega^3{Y_0}^2}{\left(1-(\frac{\omega}{\omega_n})^2\right)^2+\left(2(\zeta_e+\zeta_m)\frac{\omega}{\omega_n}\right)^2} \qquad (2.9)$$

The Parameters of the (2.9) are mentioned in section 2.1. Since $y(t) = Y_0 \sin(\omega t)$, vibration acceleration can be written in the form $y''(t) = -Y_0\omega^2 \sin(\omega t)$. Inserting the acceleration equation in (2.9), output power of the EMEH at resonance frequency can be written as (2.10).

$$P = \frac{m\zeta_e(Y_0\omega^2)^2}{4\omega_n(\zeta_e+\zeta_m)^2} \qquad (2.10)$$

Analysing equation 2.10, apart from the input vibration acceleration characteristics, the output power is directly proportional to the oscillating mass and inversely proportional to the damping factors. Thus, increasing the oscillating mass improves the output power. However, one should be careful since increasing the oscillating mass increases the oscillation displacement amplitude, which has a limit depending on the energy harvester structure. Hence designing a moving coil energy harvester is preferred since the coil structure, including the energy harvester body, has much more mass than the magnet structure.

The method in [17] is adopted to increase energy harvesting bandwidth. To determine the displacement limit, equation 2.2 can be used. At the resonance frequency, equation 2.2 becomes $z(t) = \frac{Y_0}{2(\zeta_e+\zeta_m)}\sin(\omega t - \varphi)$. Using the well-known displacement equation of $d_{peak} = \frac{a_{peak}}{4\pi^2 f^2}$, where a_{peak}=0.4 g and f=24 Hz, $d_{peak}=Y_0$=0.173 mm. For damping factors, a conventional value of $\zeta_e = \zeta_m = 0.015$ is given in [15]. Using all the findings, an oscillation peak of 2.883 mm can be calculated for the moving coil of the electromagnetic energy harvester. The proposed structure with its dimensions is given in section 2.5.1

2.5.1 3D Design of the Structure

The proposed moving coil electromagnetic energy harvester design in Figure 2.18 utilises the repulsively stacked magnet structure of [19] and improved bandwidth property of [17]. N42 neodymium magnets are used in the structure to improve magnetic flux density. Stationary cube magnets (8x8x8 mm^3) at the centre provide the magnetic flux necessary for energy harvesting according to Faraday's Law. Magnets at the top and bottom of the case and the moving coil structure determine the spring constant; in other words, they adjust the resonance frequency of the EMEH. Finally, magnets at the sides of the case and the moving coil structure provide stability to the structure and keep the moving coil structure suspended at the same resting point, which eliminates the orientation dependency of the EMEH. The coil thickness is 2 mm, and their turn numbers are 500 at the centre and 625 at the top and bottom.

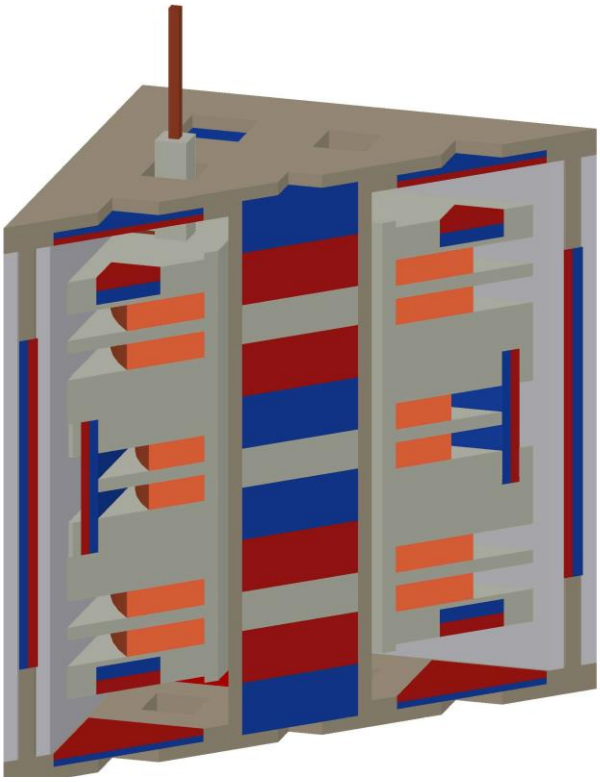

Figure 2.18. Cross-section of the designed MC-EMEH.

3D SLA printed parts of the MC-EMEH are shown in Figure 2.19. 3D Printed MC-EMEH structure with neodymium magnets.

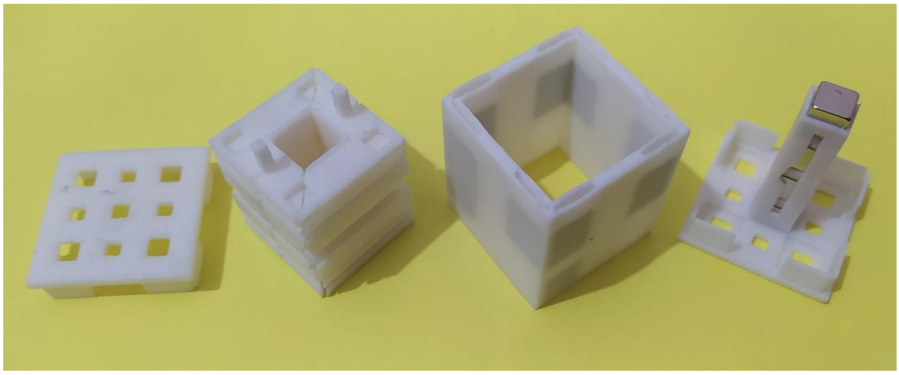

Figure 2.19. 3D Printed MC-EMEH structure with neodymium magnets.

2.5.2 FEM Model

Besides the analytical modelling of the system, finite element methodology can be used for modelling the EMEH and studying the model parameters before fabrication. For this purpose, the FEM software of COMSOL is used. The revolved simplified 3D-FEM model of the harvester is presented in Figure 2.20. The system is composed of four fixed cubic neodymium magnets with one side of 8 mm and three pairs of coils.

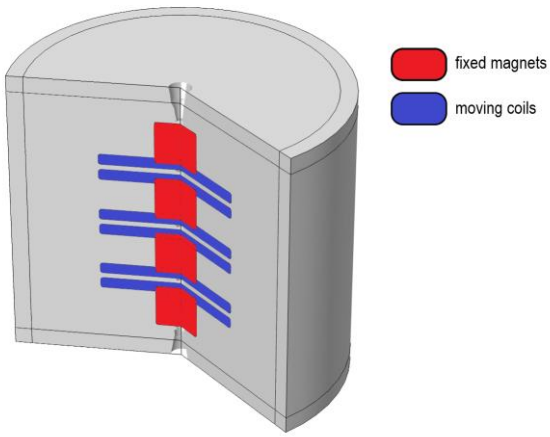

Figure 2.20. Revolved MC-EMEH FEM model.

The strongest magnets in the world and the strongest rare earth magnets are neodymium magnets; thus, N42-type neodymium magnets are preferred by also considering market availability.

The material properties of the preferred interest are presented in shows that the remnant flux density of the N42-type magnet is one of the highest; that is why it is also a good choice in terms of the induced magnetic field.

Table 2.2 shows that the remnant flux density of the N42-type magnet is one of the highest; that is why it is also a good choice in terms of the induced magnetic field.

Table 2.2 Material properties of neodymium magnets [37].

Material	**Br (mT)**	**Hc (kA/m)**	**Hci (kA/m)**	**(BH)max (kA/m)**
N42	1280	915	955	40

As coils, three copper-wire-based coil pairs are preferred. For the turn number optimisation, various parameters, including the frame dimensions, are considered. At the final optimised parameters, it is seen that turn numbers 625 (N0), 500 (N1), and 625 (N0) are optimum values from top to bottom configuration, respectively.

After main material parameters are inserted, and the CAD model is created, simulation modules are configured. For this study, a magnetic field module is used.

First, an infinite element domain is created, which describes the environment in which coils move through and create a magnetic field. During modelling, a rectangular area in the rz-plane constrained by the boundary condition "Magnetic Insulation" serves as the modelling space for this 2D axisymmetric issue, simulating a metallic enclosure presented in Figure 2.21. The software takes advantage of the moving mesh functionality to specify the movement of the coils and the surrounding air domains. Specifying the Moving Mesh interface in the coils and the air domains

above and below is sufficient because neither the coil nor the air domain surrounding it needs to deform.

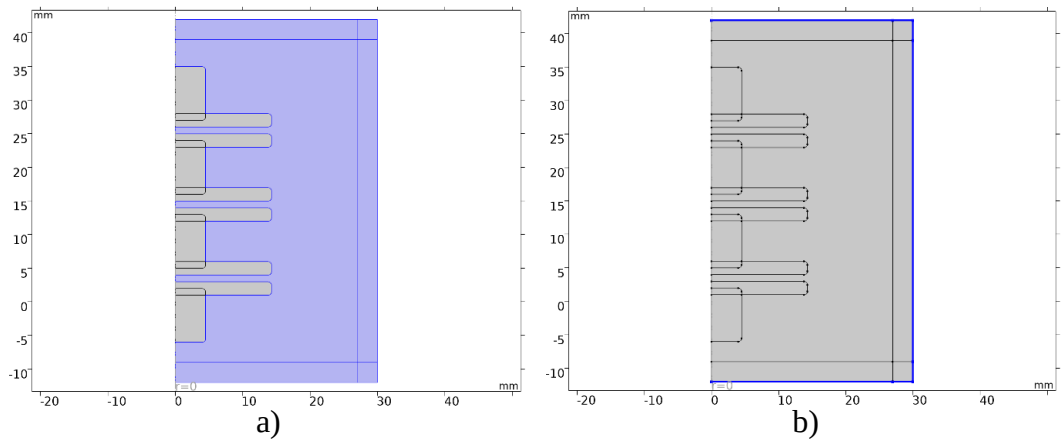

Figure 2.21. a) Infinite element domain region b) Magnetic insulation boundary region.

Rectangles are used to depict both the multi-turn coils and the magnet. The magnet and coil corners are rounded off to prevent local singularities into the magnetic fields brought on by sharp corners. By taking the integral of the fields over the domains, the induced voltage across the coil is calculated.

As a magnetisation model, the remanent flux density is preferred, and equations used during numerical solving are presented in equations 2.11 and 2.12. The magnet's flux direction is arranged in [0,0,1] and [0,0,-1] configurations in which each consecutive magnet's flux direction is opposite.

$$B = \mu_0 \, \mu_{rec} H + B_r \qquad (2.11)$$

$$B_r = \|B_r\| \frac{e}{\|e\|} \qquad (2.12)$$

The coil pair's current direction is arranged so that the top and bottom pairs have the same direction with turn numbers of 625, and the pair in the middle has a reversed current direction with a turn number of 500. Coil wire conductivity and cross-section area are 6e7 S/m and 5e-9 m^2, respectively.

The meshed model with a zoomed-up view of the finer details is presented in Figure 2.22. The meshing of the model is conducted in three steps. Magnets and coils are the domains of interest, which is why they have meshed with finer details. For these domains, free-triangular elements are preferred with a minimum element size of 16.2μm. The infinite air domain has meshed with two steps. The initial deformed domain region has meshed with eight boundary layers where each has a stretching factor of 1.2, and free quad elements are preferred for the remaining outer frame with a minimum element size of 16.2 μm. The complete meshed model is composed of 7343 triangular elements, 52 quad elements, 680 edge elements, and 78 vertex elements. The average element quality of the model is 0.8099, which is above the acceptable value.

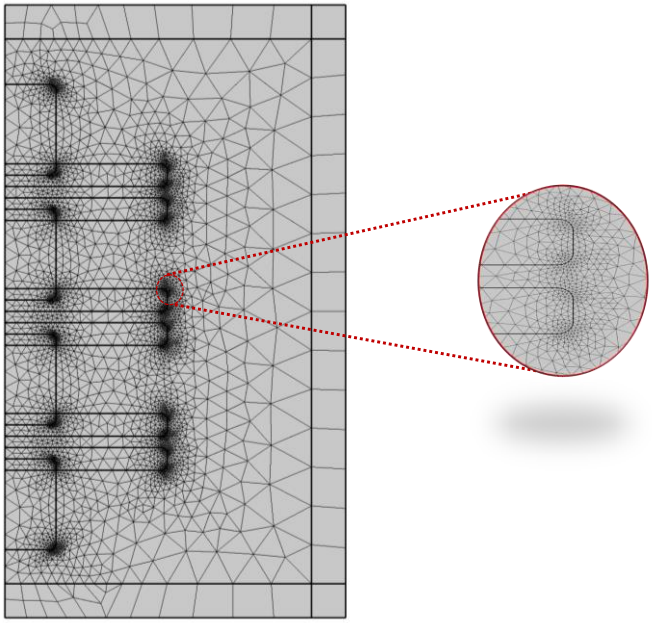

Figure 2.22. Meshed model of the 2D-axisyymmetric EMEH with zoomed up image of curved points.

The system is excited at 24.4 Hz at 0.4 g. As an input, prescribed deformation is given to the moving domains, which are coils and their closed environment. The displacement value for the coils is calculated as an input based on the displacement equation given in section 2.5.

Finally, the model is solved for two studies, stationary and time domain analysis. First, the fields owing to the magnet at its beginning location are calculated using a static analysis of merely the magnetic fields. Proper beginning conditions must be provided for the subsequent transient analysis of the magnetic fields and the moving mesh.

Figure 2.23 presents the magnetic and electric field distribution under 0.4 g excitation. It can be observed that both fields are more dominant in the corners of the magnets in which coils and magnets overlap with each other. Magnetic flux direction is as expected and opposite at each magnet, resulting in a higher magnetic field in this configuration.

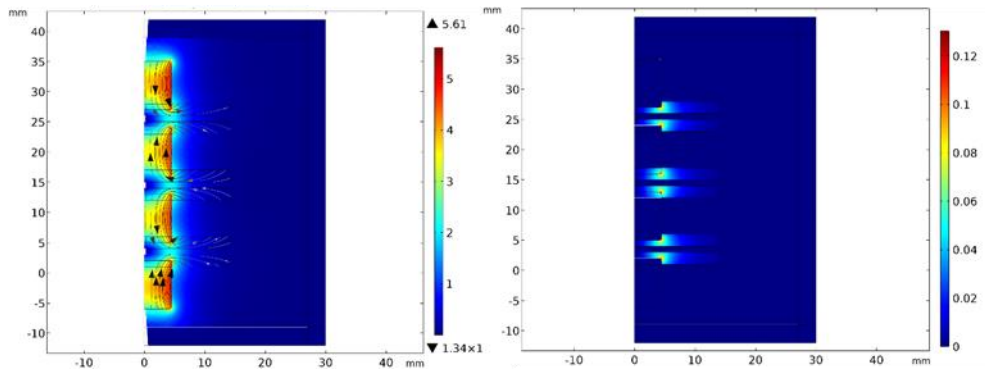

a) b)

Figure 2.23. a) Magnetic flux distribution under 0.4 g excitation b) Electric field distribution under 0.4 g excitation.

In Figure 2.24, coil voltage and harvested power are presented for 100ms. 5 V_{pp} and 9 mW power are obtained at 0.4 g, among the highest values in the literature at this footprint. Therefore, with a small-footprint design, high-voltage and high-power outputs are succeeded with this novel quadruple electromagnetic vibration energy harvester.

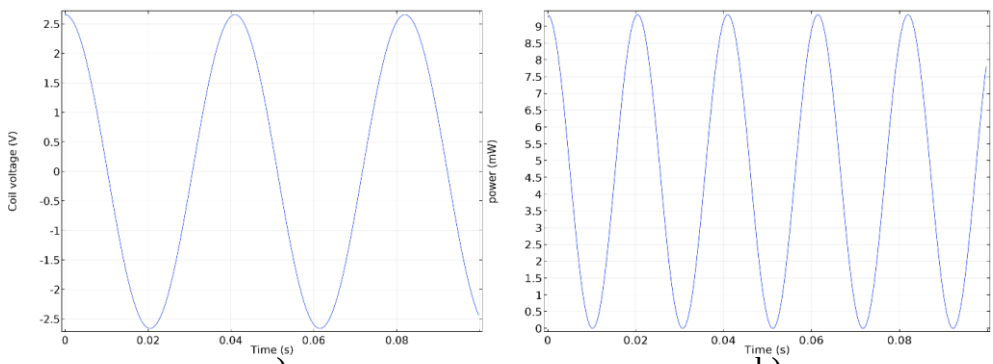

a) b)

Figure 2.24. a) Coil voltage under 0.4 g excitation b) Coil power under 0.4 g excitation.

2.5.3 Fatigue Analysis of the Electromagnetic Energy Harvester

Fatigue analysis is essential for materials which exhibit harmonic loading since this type of failure can occur at low-stress levels. Fatigue calculations using Harmonic

Analysis use Stress-Life (S-N) Method in Ansys Mechanical. This method is suitable for low-stress and high-cycle applications. Since the required S-N curve does not exist in the ANSYS Mechanical library for any ABS material, static and harmonic analysis are conducted to check the order of magnitude of the stress distribution to compare with the material's tensile strength.

This part will discuss the effect of harmonic loading that may cause fatigue failure. The device consists of three main parts. The effect of the middle part on the upper and lower caps will be similar; therefore, only the upper cap will be examined.

The excitement frequency of the middle part is specified around 20-30 Hz, which results in maximum peak-to-peak voltage and average power. The given acceleration range for this part is 0.4-1.6 g.

Modal analysis is carried out first to determine the eigenfrequencies of the cap. Considering the fixed boundary conditions at corners, six modes of the structure, together with the eigenfrequencies, are calculated. Figure 2.25 and Table 2.3 show the first three modes with deformation distributions and corresponding eigenfrequencies.

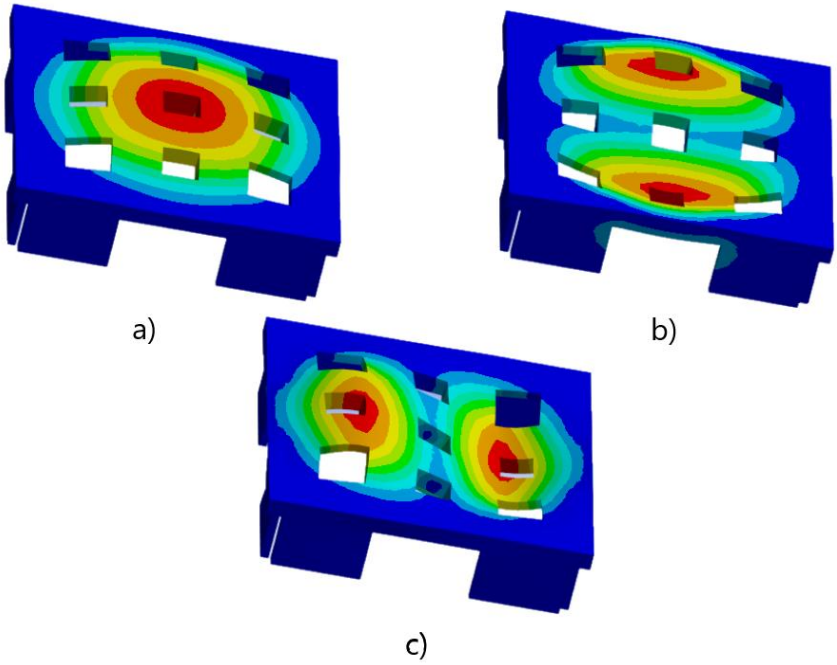

Figure 2.25. First three modes of upper cap with total deformation distribution.

Table 2.3 First three modes and corresponding eigenfrequencies.

Mode	Frequency (Hz)
1	3229.4
2	6456
3	6506.6

As Table 2.3 shows, the eigenfrequencies of the structure are way above the excitement frequency of the middle part. Because of this great difference, it can be said that the effect of the frequency does not change the results significantly, which can be observed in Figure 2.26.

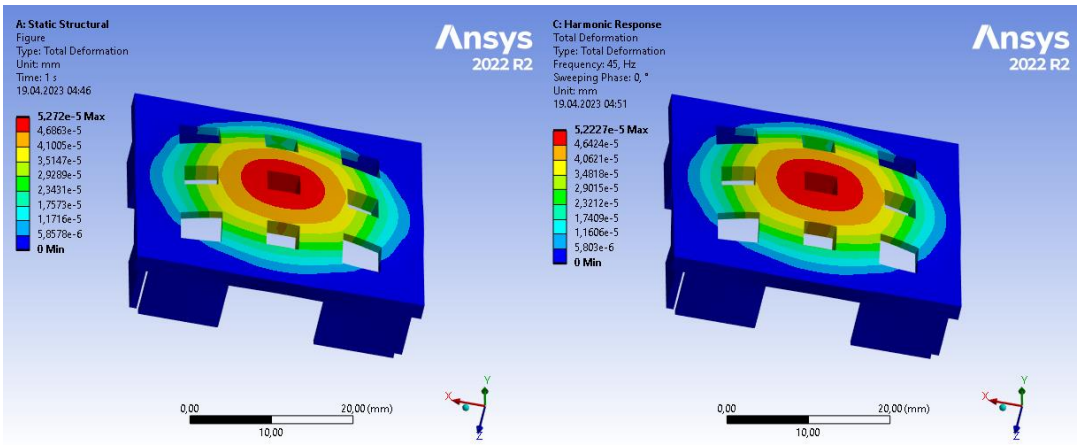

Figure 2.26. Total deformation distribution on the upper cap at a given acceleration of 1.6 g for static vs harmonic analysis.

Static structural analysis results indicate that the deformation is in the order of e-05. Therefore, it can be said that the results are almost insignificant. Harmonic analysis is made for the range of 0-45 Hz, giving almost the same result as expected.

The same comparison can be made for the equivalent stress as well. It can be seen in Figure 2.27 that the material's tensile strength (55.7 MPa) [43] is way above the obtained stresses. Therefore, fatigue analysis becomes irrelevant for this scenario.

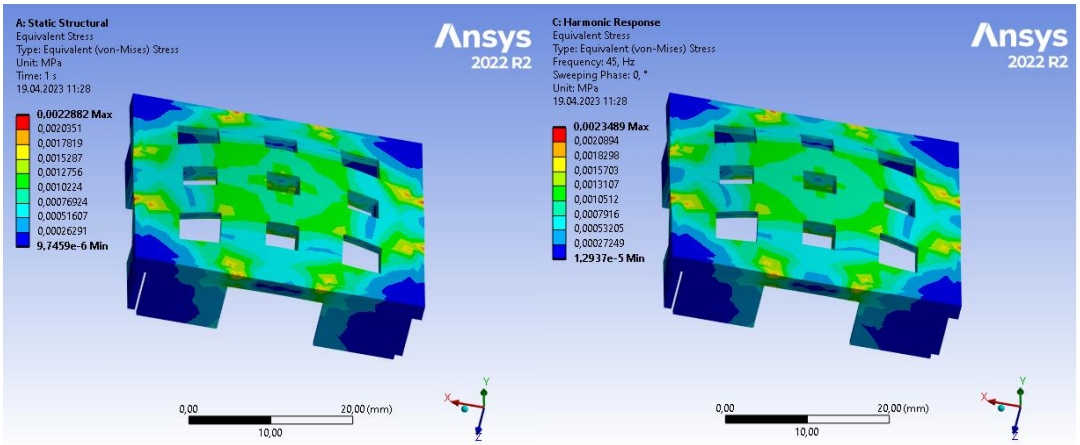

Figure 2.27. Equivalent (von-Mises) Stress distribution on the upper cap at a given acceleration of 1.6 g for static vs harmonic analysis.

CHAPTER 3

VIBRATION BASED ENERGY HARVESTER INTERFACE IC

Energy harvesting systems convert the available energy from ambient energy sources to electrical energy in either AC or DC form. DC electrical power can be obtained by harvesting energy sources such as thermal and solar. However, harvesting vibration energy sources yields AC electrical power, which can be expected from the alternating amplitude nature of the vibrations. Regardless of the energy harvesters' electrical output type, the targets of the energy harvesting, which are sensor nodes and energy storage elements (rechargeable lithium batteries and supercapacitors), require DC power. Hence, interface electronics are necessary to perform AC/DC conversion.

Nonetheless, the properties of the obtained DC power cannot satisfy all of the power supply line regulation, noise, and ripple requirements of sensor node electronics. Furthermore, battery management circuits adopt a constant current charging method to charge lithium batteries, which requires a power management circuit. Thus, a DC/DC converter block is essential to complete energy harvesting operations.

Although complete system solutions for vibration energy harvesting are present in literature, they mainly specialise according to the properties of their target energy harvesting transducer. Hence, there is room for improvement in the flexible operation ability of the energy harvesting systems: off-resonance operation, load impedance matching, and maximum power point tracking (MPPT) capabilities.

3.1 System Block Diagram of Energy Harvester Interface Electronics

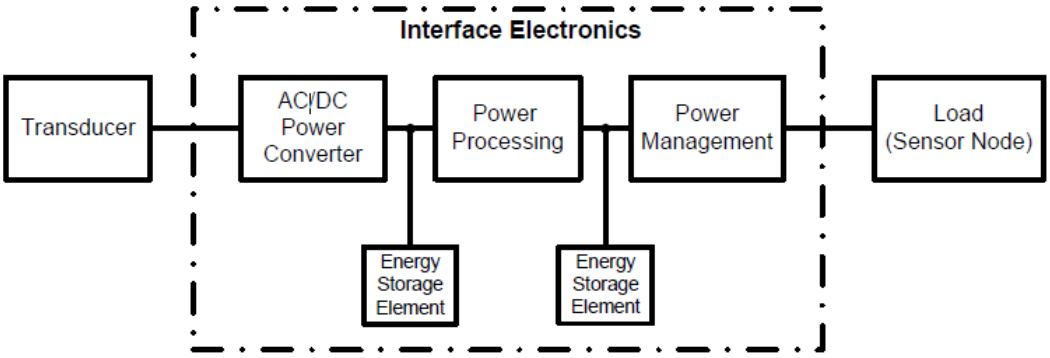

Figure 3.1. Basic interface electronic circuitry for vibration-based energy harvesters. [42]

Vibration-based energy harvesting systems aim to convert harvestable energy into DC form, and the first step of this operation is AC/DC conversion. DC power obtained in the AC/DC conversion is stored in the first intermediate energy storage element to be used in the DC/DC conversion stage. The next stage of the system is the DC/DC converter, which shifts the DC voltage level of the rectified and stored energy in the first step to the voltages required by the energy harvester interface and sensor node electronics. In the last stage of energy harvesting, energy stored in the second intermediate energy storage element by DC/DC converter is distributed to the system blocks via voltage regulators and a battery management system. These three stages of energy harvesting work properly in the presence of a sufficient input voltage level rectifiable by an AC/DC converter and stored energy that can power up the active elements of the stages. However, energy harvesting systems must power up with cold start conditions. Consequently, a power management system that contains a start-up circuit is necessary to power up energy harvesting stages and direct the input power to the corresponding stages.

3.2 AC/DC Converters

The first stage of energy harvesting is AC/DC conversion, where the AC input signal is rectified. Rectification can be performed by either a half-wave rectifier or a full-wave rectifier. Both rectifiers aim to produce a pure DC signal or a signal with some specified DC component from an AC input signal. However, full-wave rectification has some fundamental advantages over half-wave rectification. One of those advantages is having a zero-average current in the AC source, which is essential for energy harvesting applications. Having a nonzero average source current means either part of the input signal is blocked or conversion of the signal to DC is not optimal. Another advantage of full-wave rectification is that rectified signal naturally has less ripple.

Another aspect of the rectifiers is that their operation is passive or active. Passive rectifiers, mainly half-wave or full-wave diode bridge rectifiers, have the advantages of design simplicity and supply-free operation capability. However, power dissipation and voltage drop of the diodes used in the passive rectification are drawbacks for low voltage and low power applications. Using semiconductors with low voltage drops or adopting active rectification methods are some solutions to mitigate these problems. Nonetheless, active rectifiers bring these advantages at the cost of pre-charged and regulated power source requirements.

3.2.1 Passive Rectification

The full-wave diode bridge rectifier is the most simple and well-known method of passive rectification. Implementation of an on-chip full-wave bridge rectifier (FWBR) is possible with diode-connected transistors, as shown in (Figure 3.2.a). Power supply-free operation capability makes FWBR configuration suitable for cold-start operation without a pre-charged energy storage element. However, voltage loss after the rectification is two diode on voltage (V_D) or two transistor threshold voltage (V_{th}). This voltage constraint limits the minimum harvestable voltage level

and reduces the system's efficiency when 2 V_D is comparable with the input voltage level. Replacing diodes with lower V_D Schottky barrier diodes or lower V_{th} transistors reduces FWBR voltage drop without changing the topology.

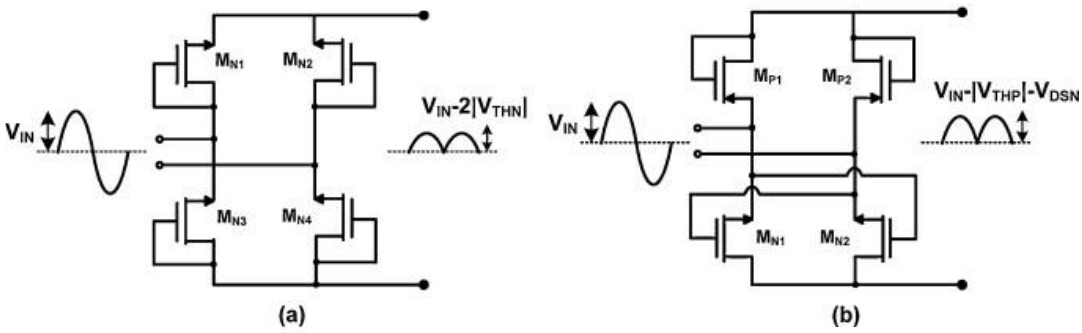

Figure 3.2. Commonly used rectifier circuit configurations: (a) full-wave bridge rectifier and (b) gate cross-coupled rectifier. [39]

To reduce FWBR voltage drop, [39] proposed a gate cross-coupled structure (Figure 3.2.b). This configuration replaces the V_{th} voltage drop of M_{N3} and M_{N4} transistors in (Figure 3.2.a) with V_{DS} voltages of the transistors which is lower than their V_{th}.

Another method to overcome the voltage drop problem of passive bridge rectifiers is using a voltage doubler circuit. The rectifier circuit in Figure 3.3 operates as a voltage doubler. When the source voltage is positive, C_1 charges to V_m-V_D through D_1; when the source voltage is negative, C_2 charges to V_m-V_D through D_2, resulting in a voltage 2(V_m-V_D) across capacitors. The advantage of the voltage doubler circuit is that for both positive and negative cycles of the source, input passes through a single diode which reduces the minimum input voltage level to V_D. Furthermore, boosting input voltage enables the system to work with low-voltage signals. In addition, capacitor values are inversely proportional to the voltage ripple of the rectified signal. Hence it is possible to generate an acceptable DC power supply for the interface electronics of the start-up system with a voltage doubler.

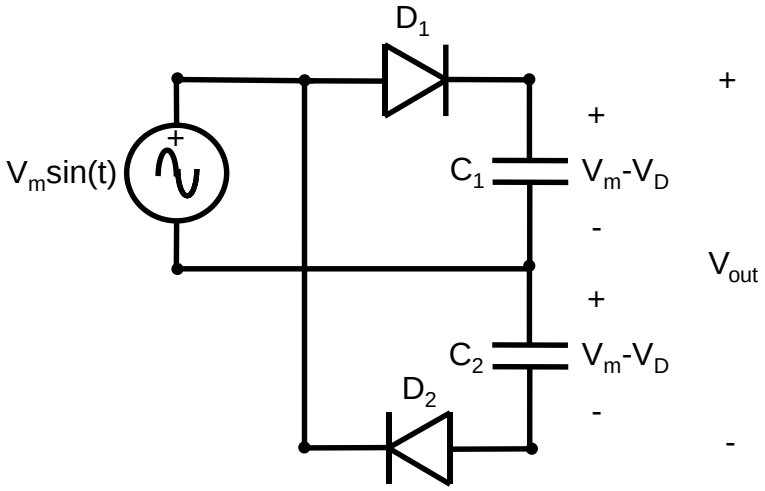

Figure 3.3. Voltage doubler circuit.

3.2.2 Active Rectification

Active rectification offers solutions for the shortcomings of the passive rectifiers mentioned in section 3.2.1. The voltage drop and power consumption problem of the passive diodes can be mitigated by using a pass transistor as a switch which is controlled by a comparator circuit. Utilising a pass transistor and comparator as an active diode results in an operation similar to an active diode, which provides significantly higher power conversion efficiency in low-voltage applications. Full-wave rectifier (FWR) in Figure 3.4 has a peak power efficiency of 86% with an 82 kΩ while a conventional passive FWBR has a 66% peak power efficiency with a 220 kΩ load [40]. Furthermore, active parts of the FWR in [40] dissipate 165 nW power, which is suitable for µ-power applications.

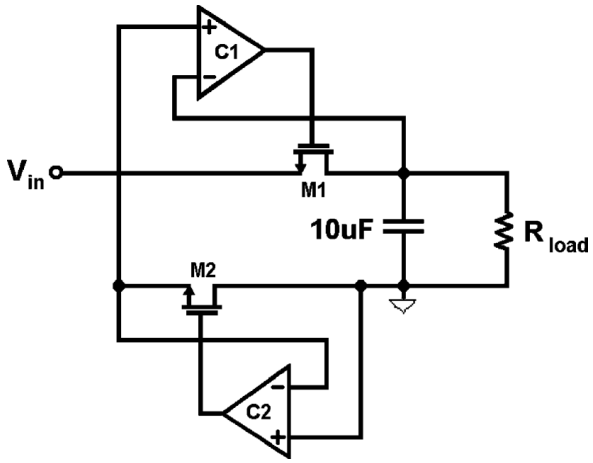

Figure 3.4. Synchronous full-wave rectifier with active diodes [2].

Another method of active rectification is by replacing diodes in a FWR with controlled switches (transistors, thyristors), resulting in topology as in Figure 3.5. When the source is positive, S_1 and S_2 will be forward-biased. Likewise, when the source is negative, S_3 and S_4 will be forward biased. However, none of the switches will conduct until an ON signal is sent to their gates. This results in a delay angle "α" that can be described as the angle interval between the forward biasing of the switches and the OFF to ON transition of the gate signals of the switches.

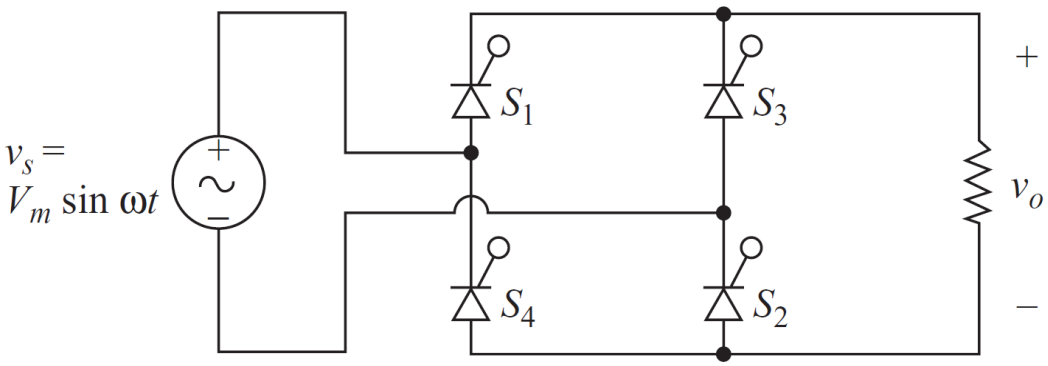

Figure 3.5. Controlled full-wave rectifier [3].

3.3 Maximum Power Point Tracking

Maximum Power Point Tracking (MPPT) is an essential technique for increasing the efficiency and effectiveness of electromagnetic energy harvesting systems. It allows for the extraction of maximum power from the energy source. The maximum power point of the system is the point on the voltage-current (V-I) characteristic of the energy source where the product of the voltage and current is at a maximum. This point can be determined experimentally by measuring the voltage and current at different operating points or by using a mathematical model of the system. There are several methods for implementing MPPT in energy harvesting systems:

Closed-loop control: In this method, a control circuit monitors the system's output power and adjusts the operating point to maintain the maximum power point. This method is relatively simple to implement, but it can be slow to respond to changes in the system's operating conditions.

Perturb and observe (P&O): This method involves periodically perturbing the system's operating point and observing the change in the output power. The operating point is then adjusted in the direction that increases output power until the maximum power point is reached. This method is relatively simple to implement but can be relatively slow to converge to the maximum power point.

Incremental conductance (INC): This method is based on the observation that the slope of the power-voltage (P-V) characteristic at the maximum power point is zero. The operating point is adjusted by incrementally changing the voltage and observing the change in current. The operating point is adjusted in the direction that results in a decrease in the slope until the maximum power point is reached. This method is relatively fast but can be relatively complex to implement.

3.4 Designed Interface Electronics

A system is designed and proposed to perform operations of a vibration-based energy harvester interface electronics explained in section 3.1. Furthermore, system blocks are designed to add the INC MPPT ability to the system mentioned in section 3.3. In this regard, a vibration-based energy harvesting system is proposed, shown in Figure 3.6.

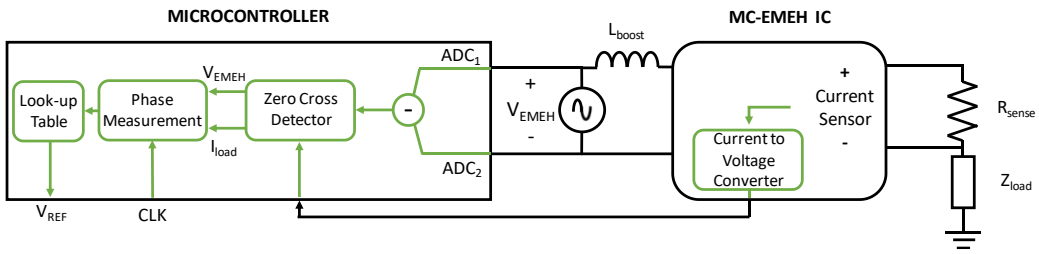

Figure 3.6. System block diagram of the proposed energy harvester interface electronics.

The core of the MC-EMEH (Moving Coil Electromagnetic Energy Harvester) is an H-Bridge structure. AC/DC conversion is done by actively controlling the switches of the H-Bridge. Moreover, by performing a chopping (PWM) operation, DC-DC conversion of the rectified signal is achieved. By implementing a control block consisting of a current sensor, hysteretic comparator, microcontroller and a gate driver, MPPT with complex conjugate impedance matching of the source and load is aimed. By measuring the load voltage and current simultaneously, phase data can be obtained. Then, using this phase data, a reference voltage V_{REF} can be generated using a look-up table. The lookup table is generated with the goal of matching the optimum load resistance of the MC-EMEH (coil resistance) and performing complex conjugate impedance matching by creating an artificial phase in the gate control signals of the H-Bridge. In the final stage of the operation, generated V_{REF} is fed to a hysteretic comparator which is connected to a gate driver circuit. Using V_{REF}, the duty cycle, frequency, and phase of the H-Bridge switching can be controlled. The gate driver circuit in the final stage controls the switch gates of the H-Bridge and ensures the break before make operation to prevent any short circuit.

3.4.1 H-Bridge structure

An H-bridge is a type of electrical circuit that may convert direct current (DC) to alternating current (AC) or vice versa. The H-bridge is made up of four bridge-style switches that can be turned on and off in various combinations to control the current flow across the circuit shown in Figure 3.7. The H-bridge can be used to rectify AC power to DC power by turning the AC waveform into a DC voltage with the same polarity as the input voltage. This is useful in applications where a DC voltage is required to power electrical components, such as a power supply. Overall, the H-bridge is a flexible circuit that may be utilised for a variety of AC-DC conversion tasks.

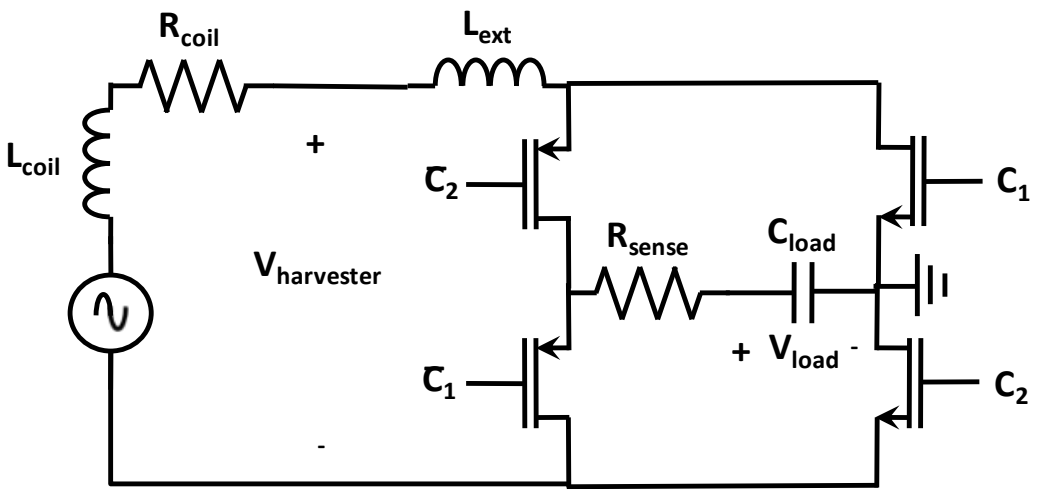

Figure 3.7. H-Bridge structure with chopping inductor (L_{ext}) and electrical model of the MC-EMEH.

The H-bridge circuit can also execute chopping operations. Chopping includes rapidly switching the output on and off to achieve a lower average output voltage. This is useful for controlling the speed of a motor or regulating the output voltage of a power source. The duty cycle of the output voltage can be modified by employing pulse-width modulation (PWM) techniques to regulate the switching of the H-bridge, which in turn changes the output voltage or motor speed.

The electrical model of the electromagnetic energy harvester consists of a series voltage source, inductance L_{coil} (68 mH) and resistance R_{coil} (380 Ω). A chopping inductor of 1 mH is selected considering the minimum inductance formula in equation 3.1 [41] to ensure continuous current operation of the system.

$$L_{min} = \frac{(1-D)R}{2f} \qquad (3.1)$$

The duty cycle will average around 50%, and load resistance R will be equal to R_{coil}=380 Ω. Finally, selecting a chopping frequency of 200 kHz well above the hearing range and compatible with the 1 Msps sampling rate of microcontroller ADCs, L_{min} is determined as 0.475 mH. Hence even if the duty cycle is close to 0%, a 1 mH chopping inductor value will be sufficient to ensure continuous current operation.

W/L ratios of H-Bridge switches are (12 mm)/(0.5 µm) for PMOS and (4.5 mm)/(0.6 µm) for NMOS. Such high W/L ratios are selected to ensure to have low ON resistances (<1 Ω) for the switches, which reduces the switching power loss of the H-Bridge structure. The layout of the H-Bridge structure is shown in Figure 3.8.

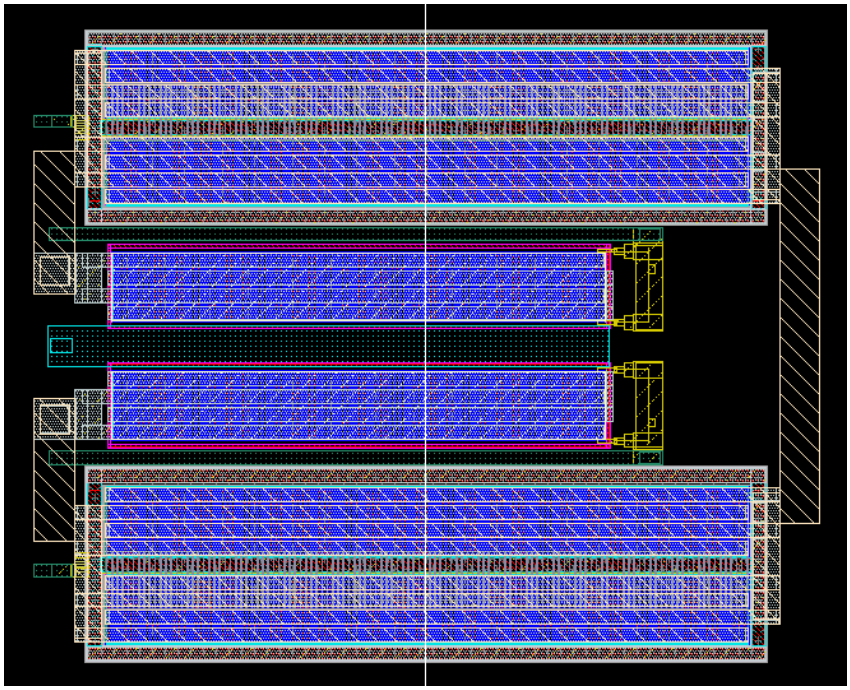

Figure 3.8. Layout of H-Bridge structure drawn using TSMC 180nm technology.

Chopping operation is performed by controlling the $C_1, \overline{C_1}, C_2, \overline{C_2}$ gate signals. C_1 and C_2 signals are also inverse during normal operation. However, the gate driver ensures that all the switches are turned off before opening other switches. Looking at Figure 3.7, it can be seen that if C_1 is high, the load capacitor is connected to a discharge path which charges the chopping inductor. Similarly, if C_1 is low, load capacitor is connected to a charge path which discharges the chopping inductor.

Layout extracted simulation of the H-Bridge structure with a 4 V source amplitude and 25 Hz source frequency is performed. The chopping frequency is matched to the input frequency to better be able to see the operation of the circuit presented in Figure 3.9.

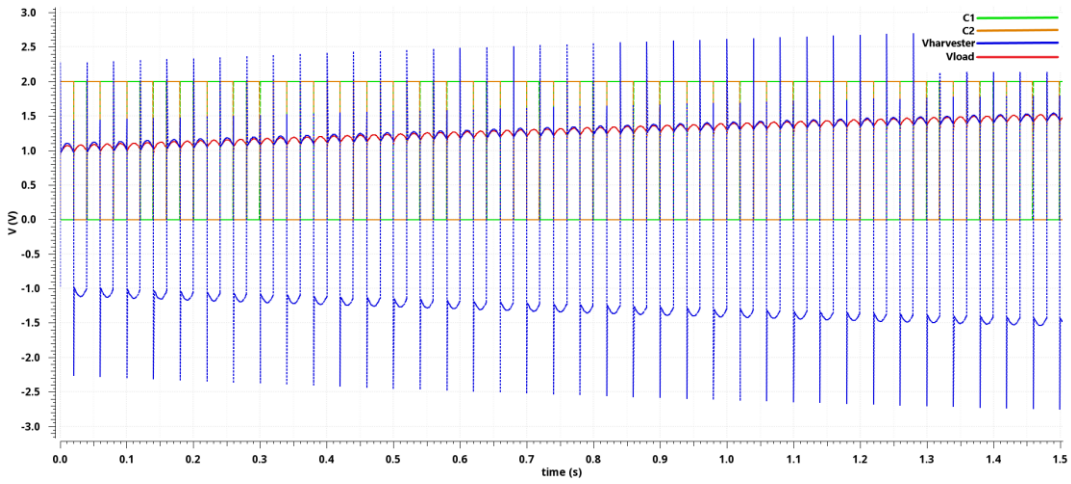

Figure 3.9. Layout extracted simulation of the H-Bridge circuit.

3.4.2 Current Sensor and Hysteresis Comparator

For the current sensor, a basic two-stage op-amp is designed, as shown in Figure 3.10. In this design transistors M_2, M_3, M_4, M_5 and M_6 have an W/L ratio of (5 µm)/(0.3 µm). Bias transistors M_1 and M_7 have an W/L ratio of (5 µm)/(2 µm).

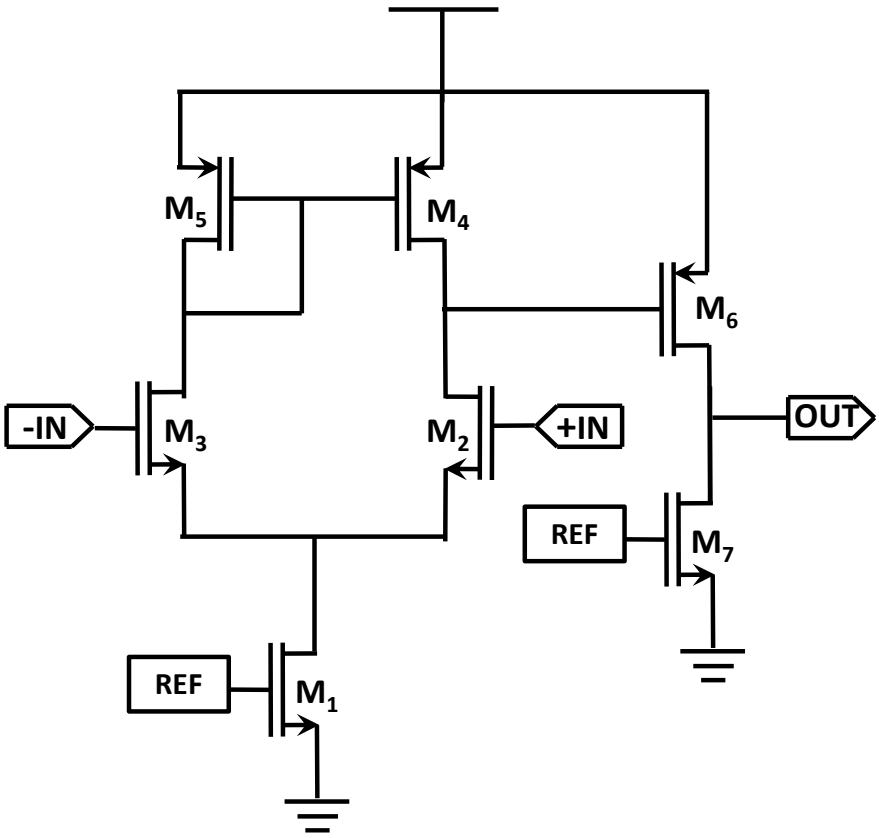

Figure 3.10. Two stage op-amp design.

Using this two-stage op-amp design, Current Sensor and Hysteresis Comparator are configured as in Figure 3.11.

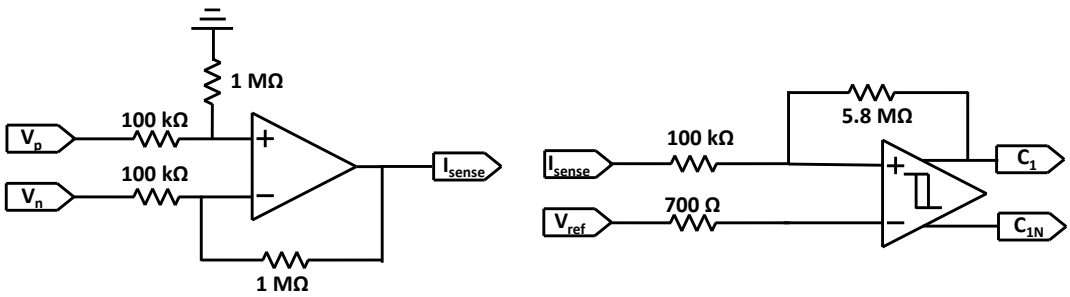

Figure 3.11. Designed Current Sensor (left) and Hysteresis Comparator (right).

The current sensor is intended to be a high-side current sensor which senses the voltage on the shunt resistor R_{sense} in Figure 3.7. When compared to low-side current sensing, high-side current sensing has various advantages. The first advantage of high-side current sensing is that it does not cause ground disturbances. When other

circuits in a system are required to connect with the load, ground disturbances are an issue. Because the shunt resistor is no longer directly linked to the ground when it is placed above the load, as in high-side current sensing, ground disturbances are eliminated. The ability to detect a load short to ground is another advantage of high-side current sensing. When using high-side current sensing, the shunt resistor remains in the circuit and can detect a surge in current from a short to ground state; however, when using low-side current sensing, the shunt resistor is removed from the circuit. This way, a short circuit protection system can be implemented to protect the interface and the battery.

The last important property of the current sensor is its frequency bandwidth. As mentioned in section 3.4.1, a chopping frequency of 200 kHz is adopted. Hence the current sensor should be stable and flat around this frequency of operation. As Figure 3.12 shows, above 1 V supply voltage, the current sensor has a flat gain of 9.8-10 V/V up to 400 kHz and a 3 dB bandwidth greater than 1 MHz.

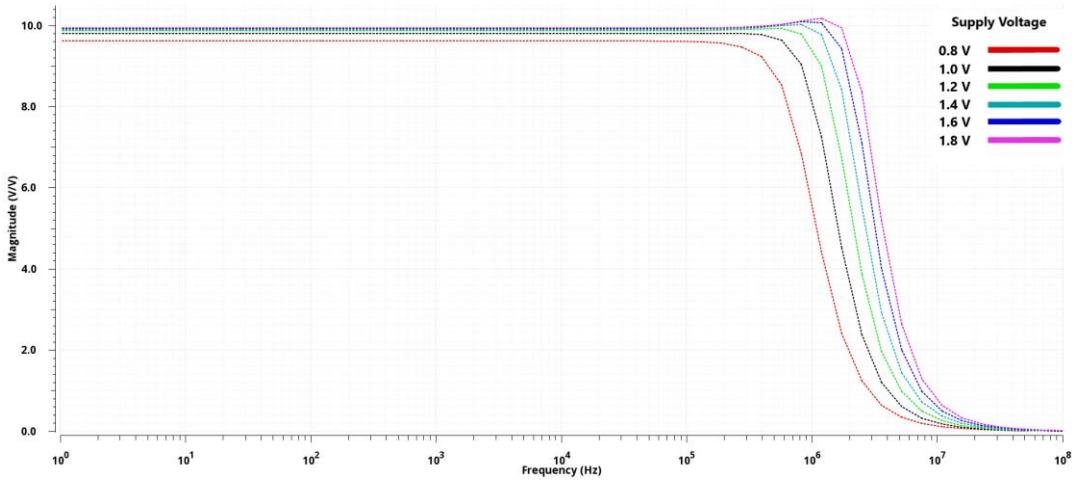

Figure 3.12. Magnitude frequency response of the designed current sensor.

The last sub-block of the system is the hysteresis comparator which completes the switching operation by controlling the gate driver of the H-bridge structure. Similar to the current sensor, the hysteresis comparator is also able to handle 200 kHz chopping frequency since the same op-amp as in the current sensor is used. The measured hysteresis curve of the hysteresis comparator for the 1.6 V supply can be

seen in Figure 3.13. The system has a hysteretic threshold of 145 mV and an offset of 17.5 mV. This offset can be handled at the MCU side by adjusting the look-up table so that the hysteresis comparator switches symmetrically.

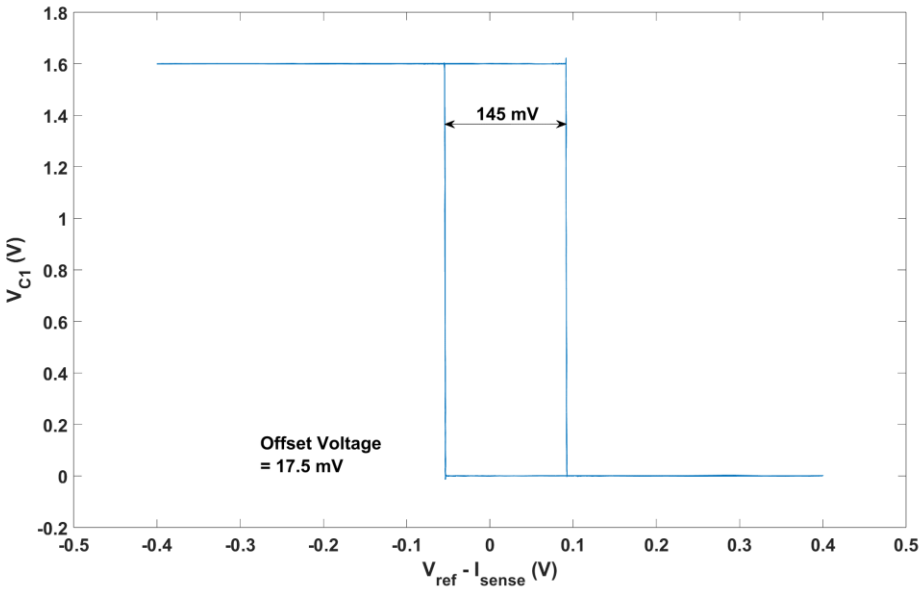

Figure 3.13. Measured hysteresis curve of the Hysteresis Comparator.

The layout of the Current Sensor and Hysteresis Comparator with their current reference is shown in Figure 3.14.

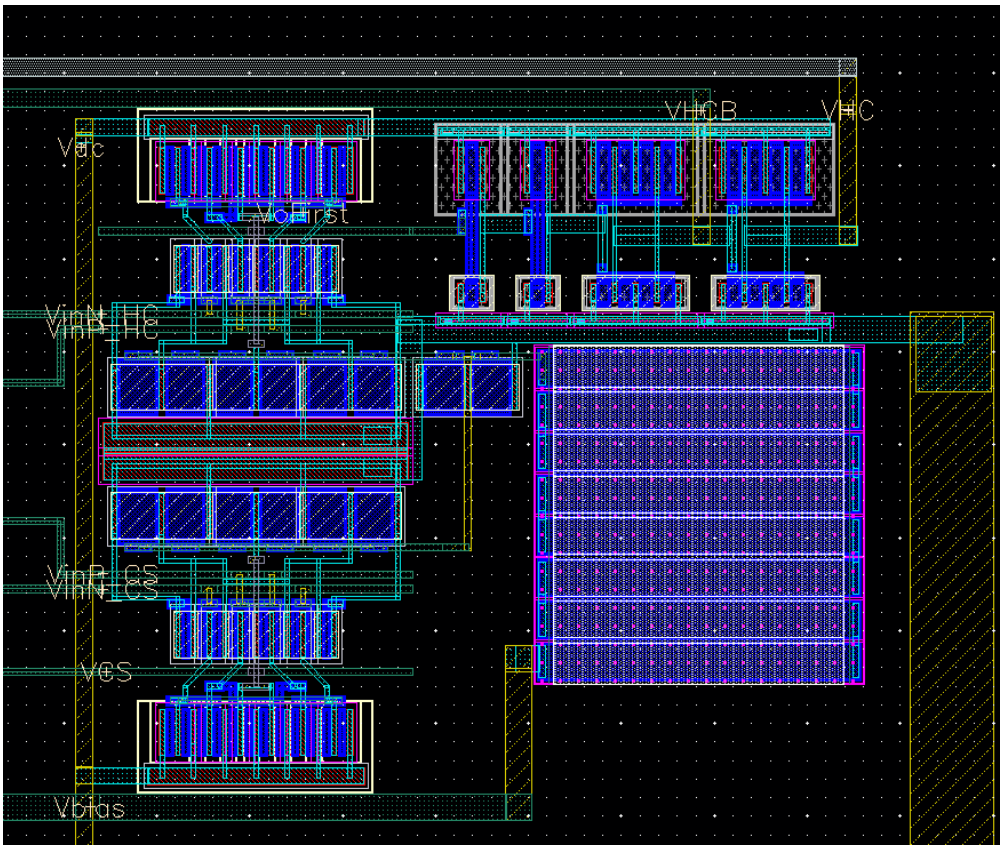

Figure 3.14. Layout of Hysteresis Comparator (top), Current Sensor (bottom left) and current reference (bottom right) drawn using TSMC 180 nm technology.

3.4.3 System Operation

The same energy harvester properties in section 3.4.1 are used in the system operation layout extracted simulation. In addition to that, from Figure 3.7, current sensor resistance R_{sense} is selected as 5 Ω and load storage capacitor C_{load} is selected as 1 mF. The current sensor is a high-speed op-amp with an inverting configuration of -10 V/V gain. DC level of the current sensor is shifted to 600 mV so that both positive and negative currents can be measured. The energy harvesting operation of the system with the current sensor is shown in Figure 3.15.

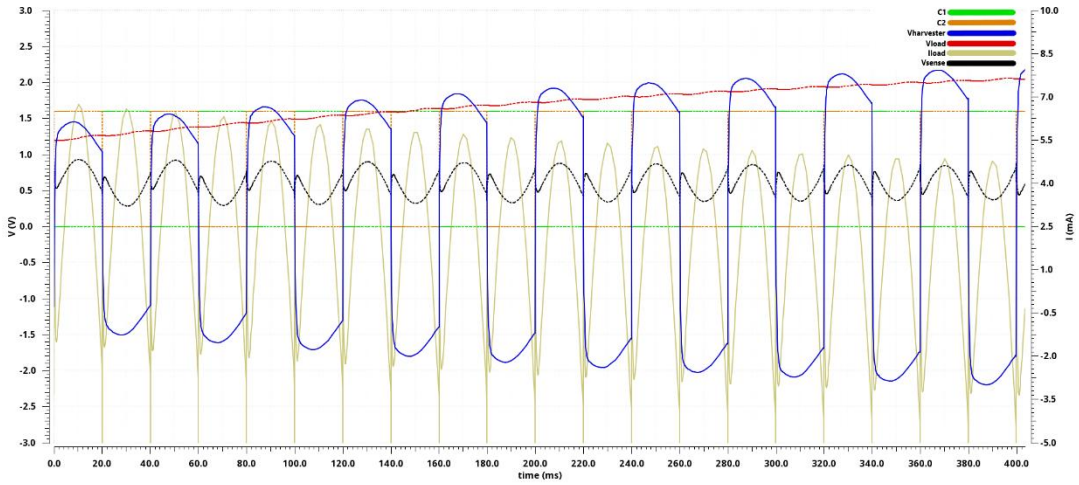

Figure 3.15. Layout extracted simulation of the H-Bridge circuit and current sensor.

The layout of the overall system is presented in Figure 3.16, and the chip photograph is shown in Figure 3.17.

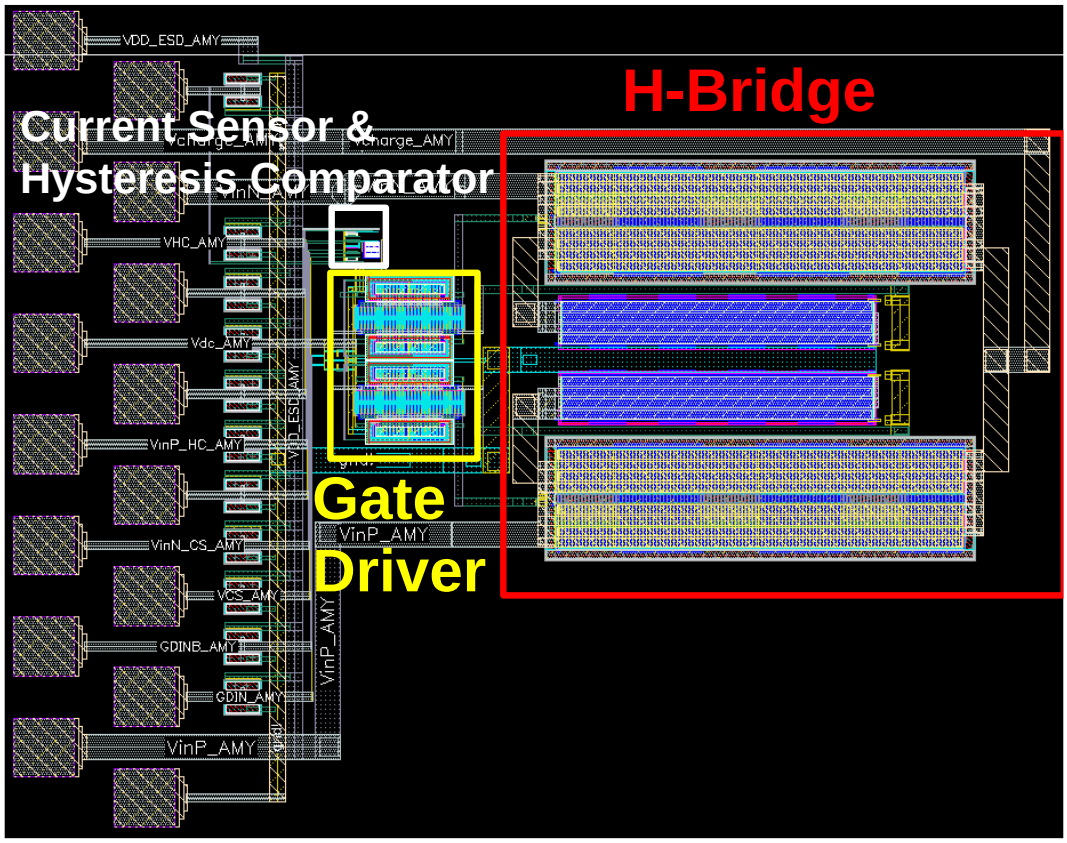

Figure 3.16. Layout of the designed interface electronics.

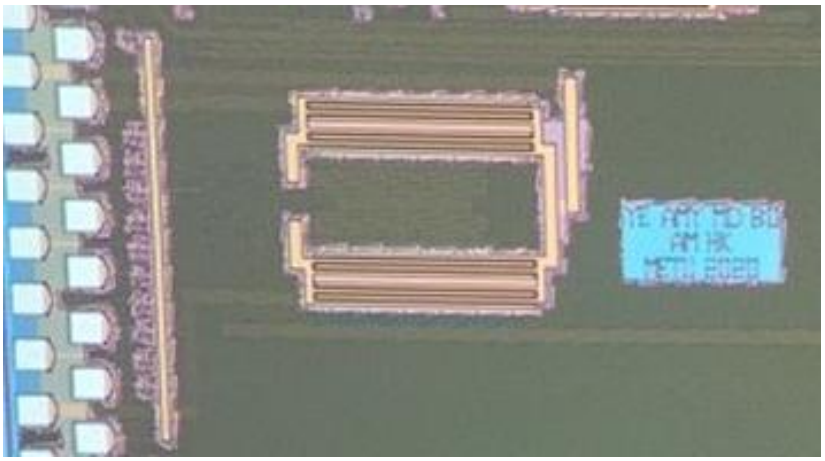

Figure 3.17. Fabricated interface circuit with TSMC 180 nm technology.

CHAPTER 4

EXPERIMENTAL TEST RESULTS

This chapter presents the experimental results and characterisation of the designed and fabircated hybrid energy harvester and MC-EMEH. Besides, a car vibration analysis is given that is used in the design process of MC-EMEH.

4.1 Transducer Characterization System

Figure 4.1 shows the “Transducer Characterization Assembly” used in the characterization and testing of EMEHs and PEHs. Vibration is provided to the shaker table via a power amplifier. This power amplifier is driven by a vibration controller, which generates the electrical output by processing the accelerometer data with “Vibration VIEW” software. Independent from the vibration control system, a data acquisition board using the NI9234 voltage measurement module acquires the measurement data and saves it in an Excel file.

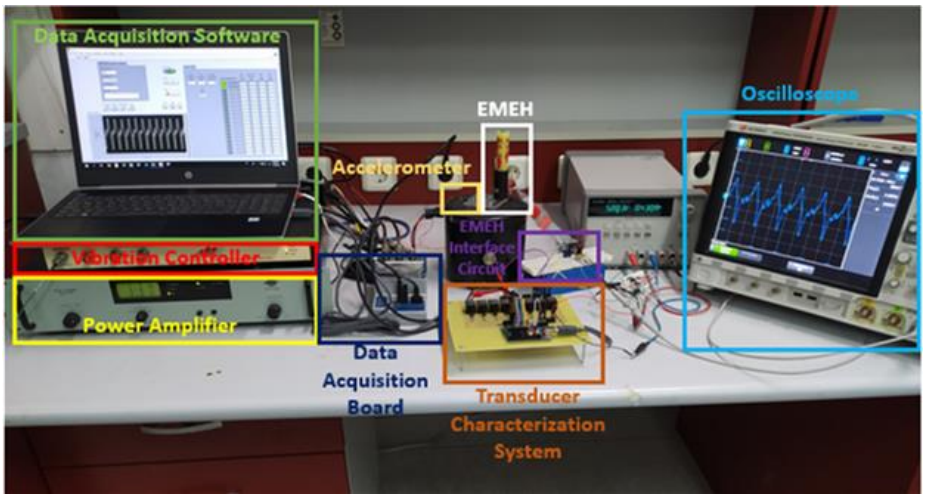

Figure 4.1. "Transducer Characterization Assembly" used in EMET and PET characterization.

Since both EMEH and PEH transducers are tested with various resistive loads to determine the optimum load resistance of the harvesters, a "Transducer Characterization System" is implemented, whose PCB layout is shown in Figure 4.2. This system is basically a relay array that generates different parallel combinations of 8 resistors. Relays are controlled by a microcontroller which is also controlled by NI LabVIEW software via USB.

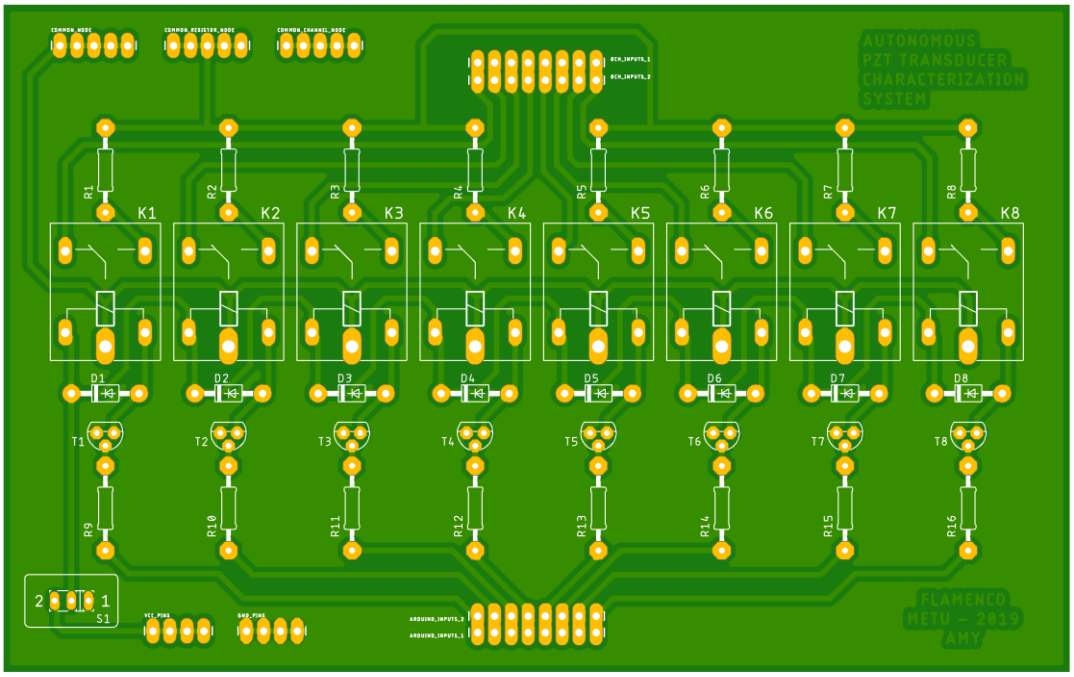

Figure 4.2. PCB Layout of the "Transducer Characterization System".

User interface of the "Transducer Characterization Assembly" can be seen in Figure 4.3. Using the interface, frequency sweep parameters and load resistances that are desired to be tested can be determined. Furthermore, measurements can be monitored and saved in an Excel file in real-time.

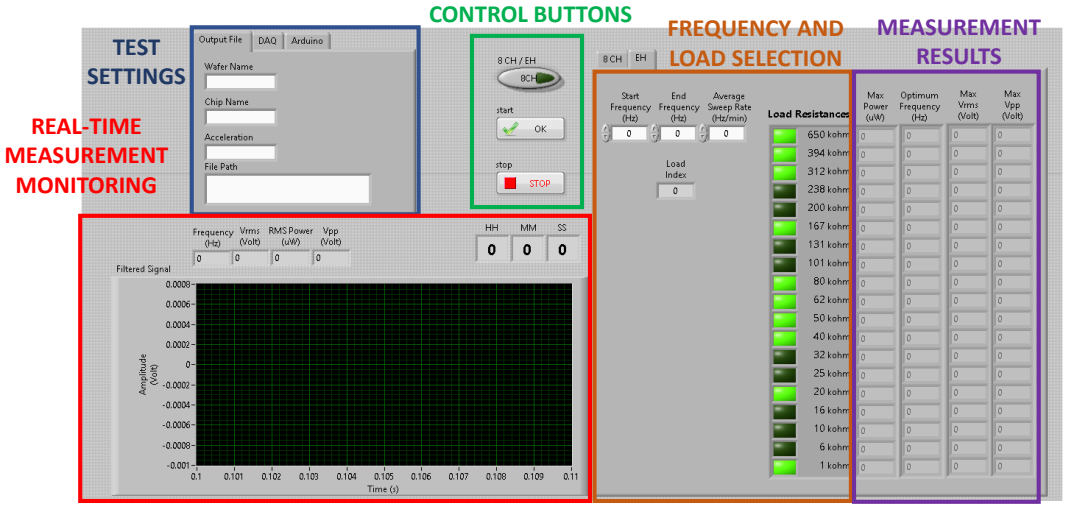

Figure 4.3. User interface of the "Transducer Characterization Assembly".

4.2 Hybrid Energy Harvester Test Results

As described in section 2.4.3, while touching the EMEH body, the PEH vibrates like a beam fixed at two ends and the stiffness is described by (2.7). This assumption is valid if the tip mass of the PEH is very large so that it fixes the tip of the beam to the EMEH body. However, this is not the case (the mass is 2.25 grams), and the stiffness of the PEH beam does not increase 64 times as predicted by equations (2.7) and (2.8). The frequency up-converted signal of the PEH can be seen in Figure 4.4. A jogging person's wrist input motion has a frequency in the range of 1.8-2 Hz. Thanks to the frequency up-conversion, the PEH (PZT in the figure) vibrates at its natural frequency of 23 Hz (when not in contact with the EMEH body) and decays after the excitation. The PEH also vibrates at about 88 Hz when in contact with the EMEH body. The PEH produces a maximum voltage of about 17 V at 23 Hz and about 2 V at 88 Hz. As the moving magnet moves, the EMEH produces a maximum voltage of about 3 V under an optimal load of 108 Ω, which is equal to the coil resistance of EMEH [44].

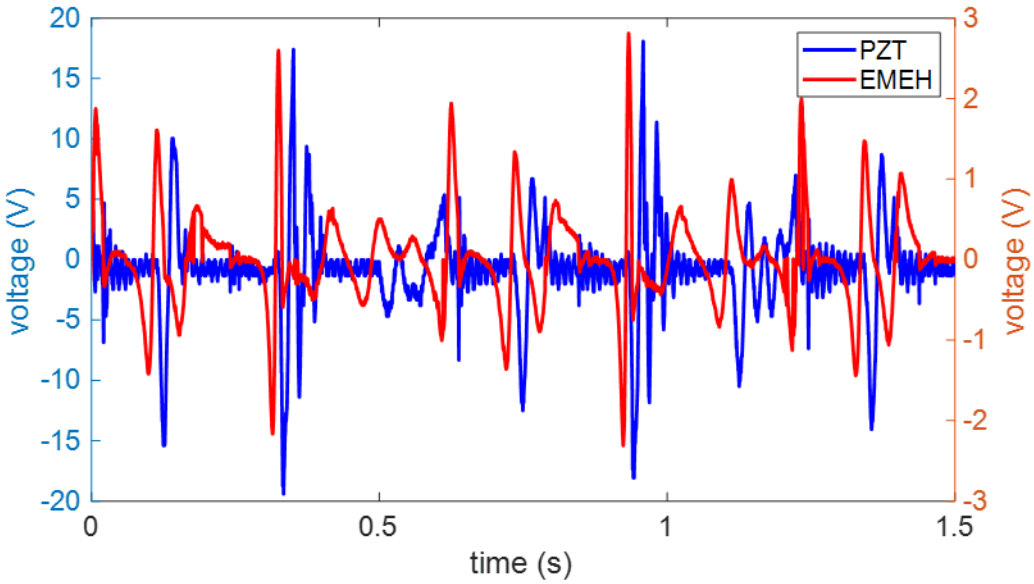

Figure 4.4. Voltage vs. Time graph of PEH and EMEH excited by wrist motion of a jogging person (acceleration in the range of 0.8-1 g at a frequency in the range of 1.8-2 Hz) at their optimum load resistances.

4.3 Hybrid Energy Harvester Test with Commercial Interface Module

There are off-the-shelf energy harvesting modules that implement solutions for different energy harvesting applications. LTC3588-1 is a module focused on harvesting energy from high source impedance energy harvesters. A schematic diagram and an application example can be seen in Figure 4.5.

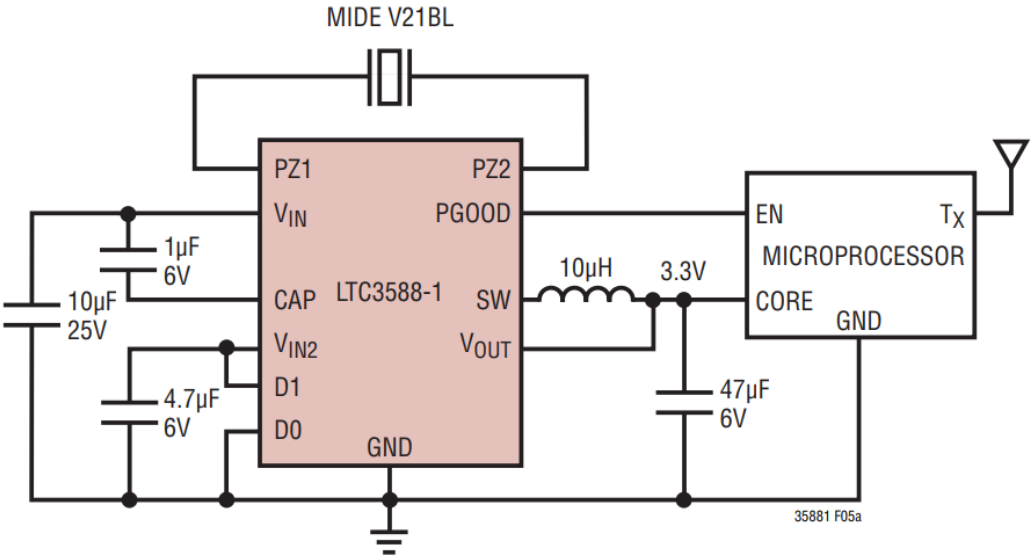

Figure 4.5. LTC3588 energy harvesting application example. [45]

Connecting the Hybrid Energy Harvester with the LTC3588-1, as shown in Figure 4.5, with a 100 kΩ load resistance, a test setup is constructed as in Figure 4.6.

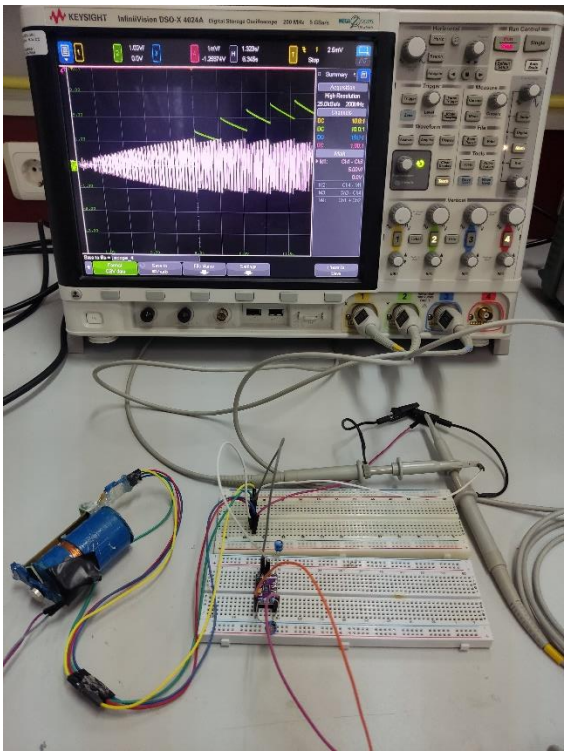

Figure 4.6. Hybrid Electromagnetic Energy Harvester test setup with LTC3588-1

Vibrating the Hybrid Energy Harvester with a running motion, a source voltage around 5 V_{peak} is obtained in Figure 4.7. As can be seen in the figure, the LTC3588-1 module stores the harvested energy and flushes to the output capacitor periodically. Since a load resistance of 100 kΩ is connected, output voltage reduces during the charging cycles. As a result, a continuous current between 20-25 µA can be supplied to the load with a 5 V_{peak} input voltage from Hybrid Energy Harvester.

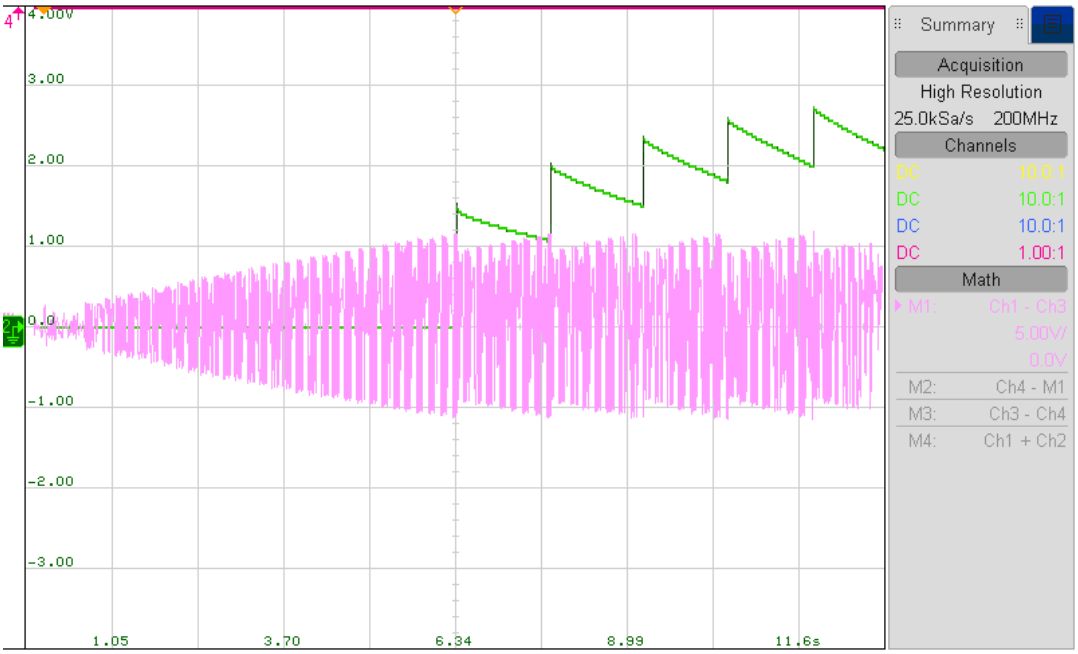

Figure 4.7. Oscilloscope output of Hybrid Energy Harvester (purple) and LTC3588-1 energy harvesting module (green).

4.4 Car Vibration Analysis

In order to design an electromagnetic energy harvester (EMEH) for vibration energy harvesting, the vibration data of a Tipo model car was analysed. By doing a power spectrum analysis and observing acceleration characteristics of vibrations, the most suitable vibration frequency range for car engine energy harvesting is selected. The engine creates a broad range of vibrations between 25-85 Hz depending on the acceleration and torque profile of the car, as shown in

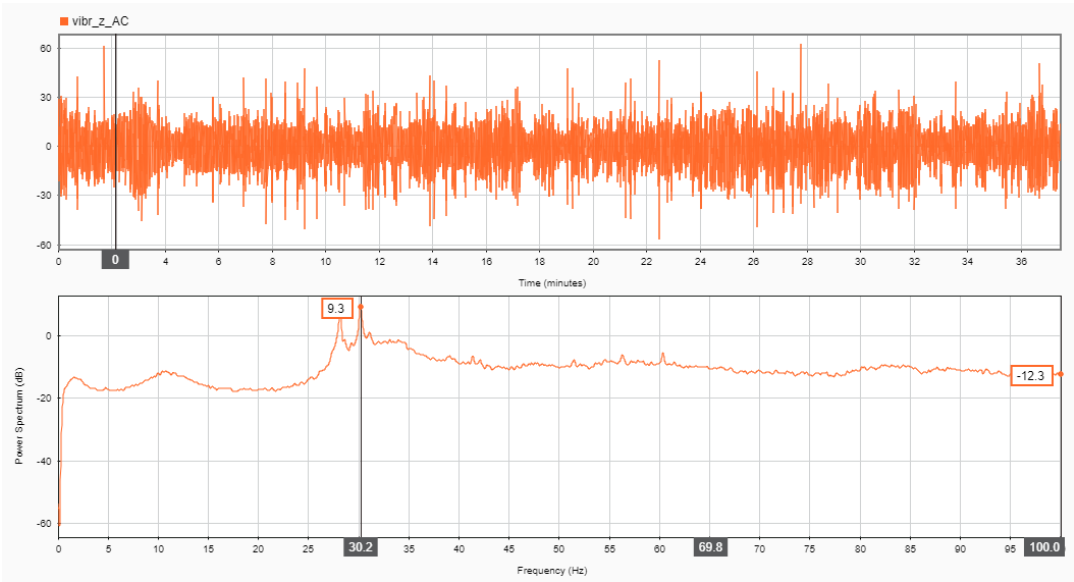

Figure 4.8. Tipo engine vibration spectrum.

The most powerful signal of the car engine is observed between 27-35 Hz frequency range, with the peak acceleration having a frequency of 30.2 Hz at 2 g_{peak} acceleration in the z-axis, as can be seen in Figure 4.9. The frequency of occurrence and constant acceleration amplitude of sinusoidal vibrations of the selected signal makes it perfect for energy harvesting applications.

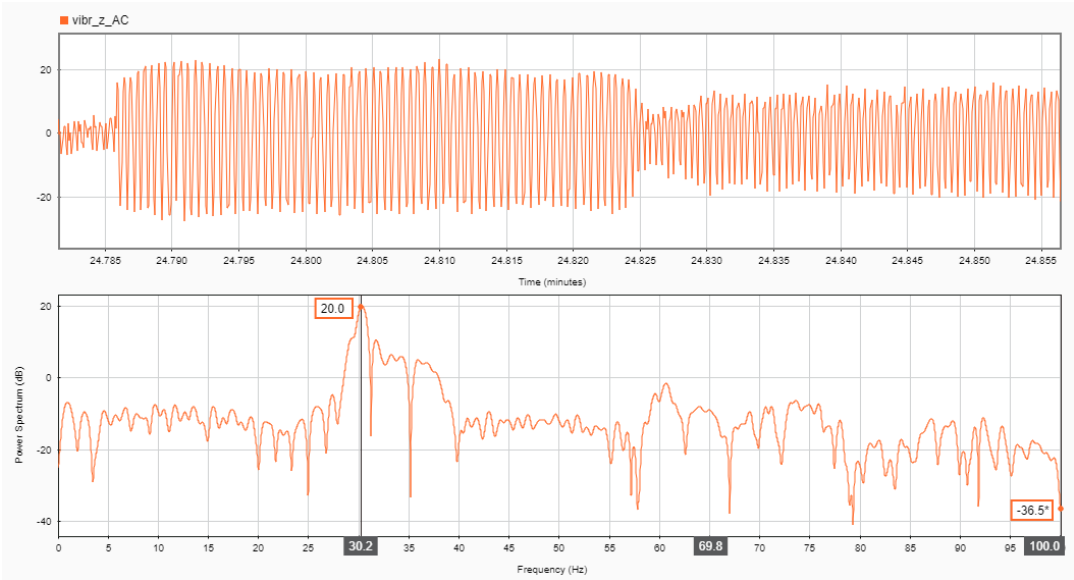

Figure 4.9. Tipo engine vibration spectrum (focused).

4.5 MC-EMEH Shaker Table Test Results

Using the test setup in Figure 4.1, MC-EMEH is tested, and an average peak power of 15.3 mW is achieved with a vibration frequency of 29.6 Hz at 1.4 g, which is slightly lower than the aimed 30.2 Hz.

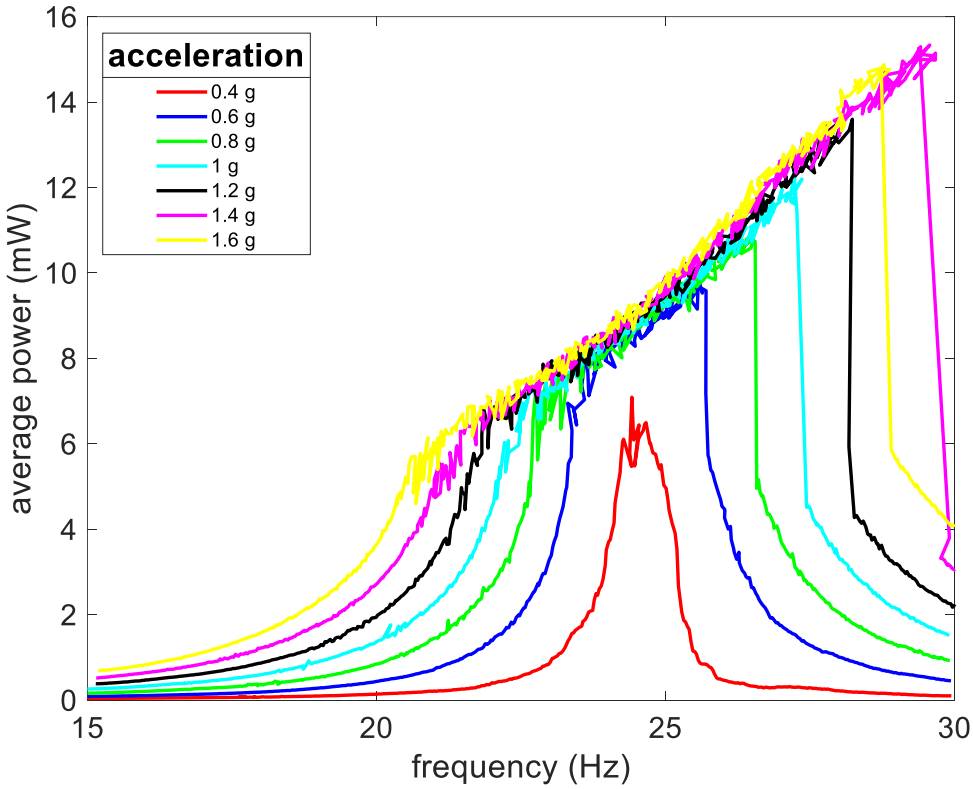

Figure 4.10. Generated average power vs. Frequency graph of MC-EMEH for 380Ω load resistance.

Performance comparison of the MC-EMEH and a commercial electromagnetic energy harvester ReVibe-ID [46] is compared in Table 4.1. Normalised power density (N.P.D.), formulated in (4.1), of the MC-EMEH, is lower than the ReVibe-ID however, this is mainly a result of the nonlinearity introduced to the MC-EMEH to improve the energy harvesting bandwidth.

$$Normalized\ Power\ Density = \frac{Peak\ Power}{Volume.Acceleration^2} \qquad (4.1)$$

The objective of this design, which is having a large energy harvesting bandwidth, is better represented with a bandwidth ratio (4.2).

$$Bandwidth\ Ratio = \frac{Half\ Power\ Bandwidth}{Center\ Frequency} \quad (4.2)$$

As Table 4.1 shows, at 1 g acceleration, bandwidth ratio of the MC-EMEH is 3.4 times that of the ReVibe-ID's. This increase in energy harvesting frequency bandwidth is crucial and makes it possible for harvesting energy from vibration sources that have varying vibration frequency such as car engines.

Table 4.1 Electromagnetic energy harvester comparison table.

Acc. (g)	*Energy Harvester*	*Center Frequency (Hz)*	*Peak Power (mW)*	*N.P.D. (mW/ cm^3/g^2)*	*Half Power Bandwidth (Hz)*	*Bandwidth Ratio*
0.4	MC-EMEH	24.4	7.1	0.797	1.2	0.049
0.4	ReVibe-ID	64.3	21.4	2.730	3.6	0.056
0.6	MC-EMEH	24.4	9.8	0.489	2.7	0.111
0.6	ReVibe-ID	64.3	44	2.494	3.7	0.058
0.8	MC-EMEH	24.4	10.9	0.306	3.9	0.160
0.8	ReVibe-ID	64.3	75	2.392	4	0.062
1	MC-EMEH	24.4	12.3	0.221	5.1	0.210
1	ReVibe-ID	64.3	110.5	2.255	4	0.062

CHAPTER 5

CONCLUSION AND FUTURE WORK

Vibration analysis for human body motions and automotive engines is performed in this thesis. Then a hybrid energy harvester and an electromagnetic energy harvester are devised, implemented, and tested. The sub-blocks of an interface electronics are then designed and produced in TSMC 180 nm technology to convert the vibration's AC voltage output to a regulated DC voltage.

This research's completed tasks and outcomes are as follows:

1. The parameters of harvestable vibrations from human body motions and car engines are identified by evaluating field data. The vibration data was then used to create energy harvesters for human wrists and automotive engines.
2. Energy harvesting issues in applications are addressed by applying proposed solutions. In this regard, a frequency up-conversion method is successfully applied in a hybrid energy harvester, and 88 Hz output voltage frequencies acquired from PEH employing 1-2 Hz human wrist motions. The other problem of constructing a broad bandwidth energy harvester for an car engine is overcome by mechanically limiting the displacement of the moving coil structure. This results in an energy harvesting bandwidth of 21-30 Hz, allowing the system to work with a variety of engine rpm values.
3. The interface electronics sub-blocks stated in Section 3 are designed in TSMC 180nm technology, and layout extracted simulations are performed. The designed system was fabricated; however the energy harvesting interface could not be implemented since the designed blocks did not operate together in the lab.

Since the designed energy harvesters show promising results for their application, future research can potentially implement the energy harvesters in their corresponding applications.

Future works that can be done are listed below:

1. Vibration analysis can be performed for other mechanical structures such as aircraft, bridges, railways and MC-EMEH can be optimized for those applications.
2. Interface electronics can be implemented with off the shelf components and tested in field to verify operation.
3. Interface electronics can be implemented with separate IC blocks and then connected outside the chip to ensure energy harvesting operation works as intended. After that, all external components can be utilised in a single compact energy harvesting chip.

REFERENCES

[1] Vailshery, L.S. (2016) *IOT devices installed Base Worldwide 2015-2025, Statista*. Available at: https://www.statista.com/statistics/471264/iot-number-of-connected-devices-worldwide/ (Accessed: April 19, 2023).

[2] *AN092 -- measuring Bluetooth Low Energy Power Consumption* (no date). Available at: https://studylib.net/doc/18071629/an092----measuring-bluetooth-low-energy-power-consumption (Accessed: April 19, 2023).

[3] *Home - stmicroelectronics* (no date). Available at: https://www.st.com/resource/en/brochure/br_wearables_rs4140.pdf (Accessed: April 19, 2023).

[4] Wan, Z.G., Tan, Y.K. and Yuen, C. (2011) "Review on Energy Harvesting and Energy Management for Sustainable Wireless Sensor Networks," *2011 IEEE 13th International Conference on Communication Technology* [Preprint]. Available at: https://doi.org/10.1109/icct.2011.6157897.

[5] Roundy, S., Wright, P.K. and Rabaey, J. (2003) "A study of low level vibrations as a power source for wireless sensor nodes," *Computer Communications*, 26(11), pp. 1131–1144. Available at: https://doi.org/10.1016/s0140-3664(02)00248-7.

[6] Chamanian, S. *et al.* (2016) "Wearable battery-less wireless sensor network with Electromagnetic Energy Harvesting System," *Sensors and Actuators A: Physical*, 249, pp. 77–84. Available at: https://doi.org/10.1016/j.sna.2016.07.020.

[7] Sajwani, H. *et al.* (2017) "Hallbach array-based linear generator for human motion energy harvesting," *2017 International Conference on Electrical and Computing Technologies and Applications (ICECTA)* [Preprint]. Available at: https://doi.org/10.1109/icecta.2017.8252017.

[8] Hehn, T. and Manoli, Y. (2015) "CMOS circuits for Piezoelectric Energy Harvesters," *Springer Series in Advanced Microelectronics* [Preprint]. Available at: https://doi.org/10.1007/978-94-017-9288-2.

[9] Jaffe, B., Cook, W.R. and Jaffe, H. (1971) "Manufacture of Piezoelectric Ceramics," *Piezoelectric Ceramics*, pp. 253–269. Available at: https://doi.org/10.1016/b978-0-12-379550-2.50015-6.

[10] Mizuno, M. and Chetwynd, D.G. (2003) "Investigation of a resonance microgenerator," *Journal of Micromechanics and Microengineering*, 13(2), pp. 209–216. Available at: https://doi.org/10.1088/0960-1317/13/2/307.

[11] Meninger, S. *et al.* (2001) "Vibration-to-electric energy conversion," *IEEE Transactions on Very Large Scale Integration (VLSI) Systems*, 9(1), pp. 64–76. Available at: https://doi.org/10.1109/92.920820.

[12] Williams, C.B. and Yates, R.B. (no date) "Analysis of a micro-electric generator for Microsystems," *Proceedings of the International Solid-State*

Sensors and Actuators Conference - Transducers '95 [Preprint]. Available at: https://doi.org/10.1109/ sensor.1995.717207.

[13] Amirtharajah, R. and Chandrakasan, A.P. (1998) "Self-powered signal processing using vibration-based power generation," *IEEE Journal of Solid-State Circuits*, 33(5), pp. 687–695. Available at: https://doi.org/10.1109/4.668982.

[14] Sterken, T. *et al.* (no date) "An electret-based electrostatic micro-generator," *Transducers '03. 12th International Conference on Solid-State Sensors, Actuators and Microsystems. Digest of Technical Papers (Cat. No.03TH8664)* [Preprint]. Available at: https://doi.org/10.1109/sensor.2003. 1217009.

[15] Spreemann, D. and Manoli, Y. (2012) *Electromagnetic vibration energy harvesting devices: Architectures, design, modeling and Optimization*. Dordrecht: Springer.

[16] Priya, S. and Inman, D.J. (2010) *Energy Harvesting Technologies*. New York: Springer.

[17] Wu, Y. *et al.* (2014) "Nonlinear vibration energy harvesting device integrating mechanical stoppers used as synchronous mechanical switches," *Journal of Intelligent Material Systems and Structures*, 25(14), pp. 1658–1663. Available at: https://doi.org/10.1177/1045389x14533437.

[18] Berdy, D. *et al.* (2012) "Low-frequency meandering piezoelectric vibration energy harvester," *IEEE Transactions on Ultrasonics, Ferroelectrics and Frequency Control*, 59(5), pp. 846–858. Available at: https://doi.org/10.1109/tuffc.2012.2269.

[19] Kwon, S.-D., Park, J. and Law, K. (2013) "Electromagnetic energy harvester with repulsively stacked multilayer magnets for low frequency vibrations," *Smart Materials and Structures*, 22(5), p. 055007. Available at: https://doi.org/10.1088/0964-1726/22/5/055007.

[20] Yasar, O. *et al.* (2018) "Optimization of AA-battery sized electromagnetic energy harvesters: Reducing the resonance frequency using a non-magnetic inertial mass," *IEEE Sensors Journal*, 18(11), pp. 4509–4516. Available at: https://doi.org/10.1109/jsen.2018.2819194.

[21] Zorlu, Ö., Topal, E.T. and Kulah, H. (2011) "A vibration-based electromagnetic energy harvester using mechanical frequency up-conversion method," *IEEE Sensors Journal*, 11(2), pp. 481–488. Available at: https://doi.org/10.1109/jsen.2010.2059007.

[22] Liu, H., Jin, L. and Gao, S. (2017) "Design and test on the nonlinear piezoelectric-electromagnetic hybrid energy harvesting structure," *2017 IEEE International Conference on Manipulation, Manufacturing and Measurement*

on the Nanoscale (3M-NANO) [Preprint]. Available at: https://doi.org/10.1109/3m-nano.2017.8286317.

[23] Hamaguchi, T. (2002) "Vibration generator for notification and portable communication device using the Vibration Generator," *The Journal of the Acoustical Society of America*, 111(3), p. 1149. Available at: https://doi.org/10.1121/1.1469272.

[24] Galchev, T. *et al.* (2011) "Energy harvesting of radio frequency and vibration energy to enable wireless sensor monitoring of Civil Infrastructure," *SPIE Proceedings* [Preprint]. Available at: https://doi.org/10.1117/12.880174.

[25] Guilar, N.J. *et al.* (2009) "An energy-aware multiple-input power supply with charge recovery for energy harvesting applications," *2009 IEEE International Solid-State Circuits Conference - Digest of Technical Papers* [Preprint]. Available at: https://doi.org/10.1109/isscc.2009.4977426.

[26] Ambrosio, R. *et al.* (2015) "Energy harvesting combining three different sources for low power applications," *2015 12th International Conference on Electrical Engineering, Computing Science and Automatic Control (CCE)* [Preprint]. Available at: https://doi.org/10.1109/iceee.2015.7357943.

[27] Uluşan, H. *et al.* (2017) "A triple hybrid micropower generator with simultaneous multi-mode Energy Harvesting," *Smart Materials and Structures*, 27(1), p. 014002. Available at: https://doi.org/10.1088/1361-665x/aa8a09.

[28] Bandyopadhyay, S. and Chandrakasan, A.P. (2012) "Platform Architecture for solar, thermal, and vibration energy combining with MPPT and single inductor," *IEEE Journal of Solid-State Circuits*, 47(9), pp. 2199–2215. Available at: https://doi.org/10.1109/jssc.2012.2197239.

[29] Katic, J., Rodriguez, S. and Rusu, A. (2018) "A high-efficiency energy harvesting interface for implanted biofuel cell and thermal harvesters," *IEEE Transactions on Power Electronics*, 33(5), pp. 4125–4134. Available at: https://doi.org/10.1109/ tpel.2017.2712668.

[30] Chamanian, S. *et al.* (2019) "Power-efficient hybrid energy harvesting system for harnessing ambient vibrations," *IEEE Transactions on Circuits and Systems I: Regular Papers*, 66(7), pp. 2784–2793. Available at: https://doi.org/10.1109/ tcsi.2019.2900574.

[31] Chamanian, S. *et al.* (2016) "Wearable battery-less wireless sensor network with Electromagnetic Energy Harvesting System," *Sensors and Actuators A: Physical*, 249, pp. 77–84. Available at: https://doi.org/10.1016/j.sna.2016. 07.020.

[32] Vokoun, D. *et al.* (2009) "Magnetostatic interactions and forces between cylindrical permanent magnets," *Journal of Magnetism and Magnetic*

Materials, 321(22), pp. 3758–3763. Available at: https://doi.org/10.1016/j.jmmm.2009.07.030.

[33] Benham, P.P. and Crawford, R.J. (1996) *Mechanics of Engineering Materials*. Harlow, Essex, England: Longman Group.

[34] *Volture datasheet V19 - tande* (no date). Available at: https://www.tande.com.tw/eh-energy-harvesting/Volture_Datasheet_001.pdf (Accessed: April 19, 2023).

[35] Lei, Y., Wen, Z. and Chen, L. (2014) "Simulation and testing of a micro electromagnetic energy harvester for self-powered system," *AIP Advances*, 4(3), p. 031303. Available at: https://doi.org/10.1063/1.4861208.

[36] Hasani, M. and Irani Rahaghi, M. (2022) "The optimization of an electromagnetic vibration energy harvester based on developed electromagnetic damping models," *Energy Conversion and Management*, 254, p. 115271. Available at: https://doi.org /10.1016/j.enconman.2022. 115271.

[37] *NDFEB magnet grades* (2022) *Bunting - eMagnets*. Available at: https://e-magnetsuk.com/introduction-to-neodymium-magnets/grades-of-neodymium/ (Accessed: April 19, 2023).

[38] Williams, C.B. and Yates, R.B. (1996) "Analysis of a micro-electric generator for Microsystems," *Sensors and Actuators A: Physical*, 52(1-3), pp. 8–11. Available at: https://doi.org/10.1016/0924-4247(96)80118-x.

[39] Rahimi, A. *et al.* (2012) "An electromagnetic energy harvesting system for low frequency applications with a passive interface ASIC in standard CMOS," *Sensors and Actuators A: Physical*, 188, pp. 158–166. Available at: https://doi.org/10.1016/ j.sna.2012.03.019.

[40] Le, T.T. *et al.* (2006) "Piezoelectric Micro-Power Generation Interface Circuits," *IEEE Journal of Solid-State Circuits*, 41(6), pp. 1411–1420. Available at: https://doi.org/ 10.1109/jssc.2006.874286.

[41] Hart, D.W. (2011) *Power Electronics*. New York: McGraw-Hill.

[42] Ulusan, H. *et al.* (2015) "A fully integrated and battery-free interface for low-voltage electromagnetic energy harvesters," *IEEE Transactions on Power Electronics*, 30(7), pp. 3712–3719. Available at: https://doi.org/10.1109/tpel. 2014.2344915.

[43] *What's The right resin for sla? 3D printing materials compared* (no date) *Hubs*. Available at: https://www.hubs.com/knowledge-base/sla-3d-printing-materials-compared/ (Accessed: April 19, 2023).

[44] Spreemann, D. *et al.* (2008) "Numerical optimization approach for resonant electromagnetic vibration transducer designed for random vibration," *Journal of Micromechanics and Microengineering*, 18(10), p. 104001. Available at: https://doi.org/10.1088/0960-1317/18/10/104001.

[45] *LTC3588-1 - nanopower energy harvesting power supply - analog devices* (no date). Available at: https://www.analog.com/media/en/technical-documentation/data-sheets/35881fc.pdf (Accessed: April 20, 2023).

[46] *MODELD product manual* (2021) *Revibe Energy*. Available at: https://revibeenergy.com/wp-content/uploads/2019/03/ReVibeEnergy_General.pdf (accessed April 24, 2023).